

GaiaUnlimited: The old stellar disc of the Milky Way as traced by the Red Clump

Shourya Khanna¹, Jie Yu^{2,3}, Ronald Drimmel¹, Eloisa Poggio¹, Tristan Cantat-Gaudin⁴, Alfred Castro-Ginard⁵, Evgeny Kurbatov⁶, Vasily Belokurov⁶, Anthony Brown⁵, Morgan Fouesneau⁴, Andrew Casey^{7,8}, and Hans-Walter Rix⁴

¹ INAF - Osservatorio Astrofisico di Torino, via Osservatorio 20, 10025 Pino Torinese (TO), Italy
e-mail: shourya.khanna@inaf.it

² School of Computing, Australian National University, Acton, ACT 2601, Australia.
e-mail: jie.yu@anu.edu.au

³ Research School of Astronomy & Astrophysics, Australian National University, Cotter Rd., Weston, ACT 2611, Australia

⁴ Max Planck Institute for Astronomy, Königstuhl 17, 69117 Heidelberg, Germany

⁵ Leiden Observatory, Leiden University, Einsteinweg 55, 2333 CC Leiden, The Netherlands

⁶ Institute of Astronomy, University of Cambridge, Madingley Road, Cambridge, CB30HA, UK

⁷ School of Physics and Astronomy, Monash University, Clayton VIC 3800, Australia

⁸ Center for Computational Astrophysics, Flatiron Institute, 162 5th Avenue, New York City, New York

Received ; accepted

ABSTRACT

We present an exploration of the Milky Way’s structural parameters using an all-sky sample of RED CLUMP (RC) giants to map the stellar density from the inner to the outer parts of the Galactic disc. These evolved giants are considered to be standard candles due to their low intrinsic variance in their absolute luminosities, allowing us to estimate their distances with reasonable confidence. We exploit all-sky photometry from the AllWISE mid-infrared survey and the Gaia survey, along with astrometry from Gaia Data Release 3 and recent 3D extinction maps, to develop a probabilistic scheme in order to select with high confidence RC-like stars. Our curated catalogue contains about 10 million sources, for which we estimate photometric distances based on the WISE W1 photometry. We then derive the selection function for our sample, which is the combined selection function of sources with both *Gaia* and *AllWISE* photometry. Using the distances and accounting for the full selection function of our observables, we are able to fit a two-disc, multi-parameter model to constrain the scale height (h_z), scale-length (R_d), flaring, and the relative mass ratios of the two disc components. We illustrate and verify our methodology using mock catalogues of RC stars. We find that the RC population is best described by a flared thin disc with scale length $R_d = 3.56 \pm 0.32$ kpc and scale height at the Sun of $h_{z,\odot} = 0.17 \pm 0.01$ kpc, and a shorter and thicker disc with $R_d = 2.59 \pm 0.11$ kpc, $h_{z,\odot} = 0.45 \pm 0.11$ kpc, with no flare. The thicker disc constitutes 64% of the RC stellar mass beyond 3 kpc, while the thin disc shows evidence of being warped beyond 9 kpc from the Galactic center. The residuals between the predicted number density of RC stars from our axisymmetric model and the measured counts show possible evidence of a two-armed spiral perturbation in the disc of the Milky Way.

Key words. Galaxy: structure – Galaxy: disc – Galaxy: fundamental parameters – Stars: distances

1. Introduction

Our Galaxy presents a unique opportunity to study the properties and distribution of millions of individual stars in detail. Over the past few decades, this has been made possible in large part thanks to high-quality photometric surveys such as *2MASS* and *WISE* (Skrutskie et al. 2006; Wright et al. 2010), spectroscopic surveys such as *Gaia*-ESO, *APOGEE*, *LAMOST*, and *GALAH* (Randich et al. 2013; Majewski et al. 2017; Steinmetz et al. 2020; Deng et al. 2012; De Silva et al. 2015), and more recently with additional synergy from the astrometry of the *Gaia* mission with unprecedented precision (Gaia Collaboration et al. 2016). The wealth of data allows us to compare how various stellar populations trace the structure and shape of the Galaxy.

The generally accepted view is that the stellar content of the Milky Way is distributed along exponential discs in the Galactocentric cylindrical coordinates (R, Z_{GC}). Early studies of stellar counts showed that the disc could be principally split into two components: a ‘thick’ disc with scale-height at the Sun of $h_{z,\odot} \sim 0.7 - 0.9$ kpc, and a ‘thin’ disc with a shorter scale-height

$h_{z,\odot} \sim 0.3$ kpc (Yoshii 1982; Gilmore & Reid 1983; Jurić et al. 2008). Conversely, the ‘thick’ disc has a shorter scale length of the two, but typical estimates range between $2 < R_d < 4$ kpc (see Bland-Hawthorn & Gerhard 2016, for full review). Large-scale spectroscopic surveys have allowed further dissection of the disc using chemistry ($[\text{Fe}/\text{H}], [\alpha/\text{Fe}]$), showing that the scale parameters vary with age (Hayden et al. 2015). For example, Bovy et al. (2016) analysed *APOGEE* data in bins of mono-abundance (\sim mono-age population), and found that the radial density of the high $[\alpha/\text{Fe}]$ population can be described by a single exponential over a large range in Galactocentric radius R . The low $[\alpha/\text{Fe}]$ population instead exhibits more complex radial density profiles and it is understood as a series of sub-discs of similar ages, peaking in density at different radii from the inner to the outer disc.

In order to simultaneously model the vertical and radial structure of the disc, it would be advantageous to use a population of stars that is numerous, spans a large range in R , and for which distances can be reliably derived. To this end, in this paper, we use stars in the RC evolutionary phase. These are low-

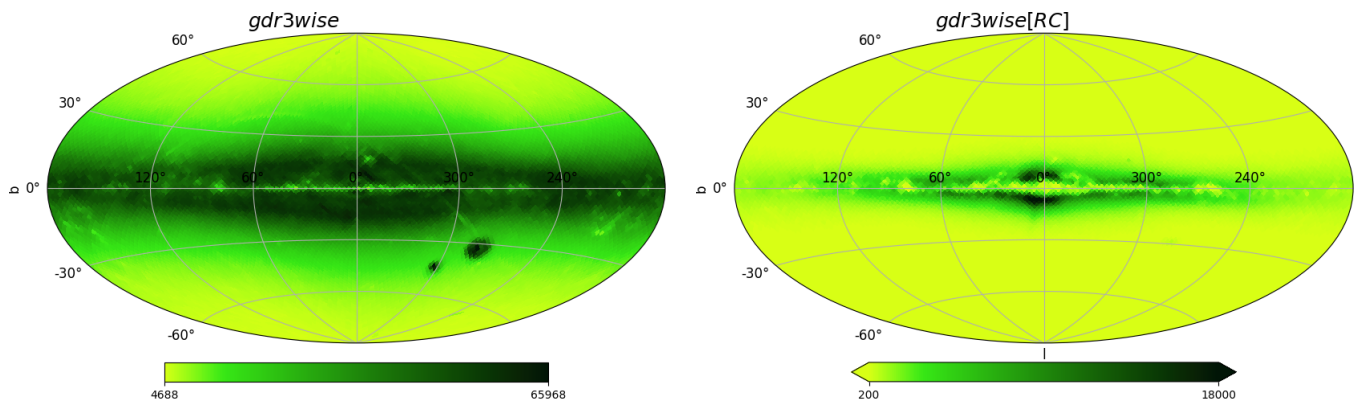


Fig. 1. All sky spatial distribution of our dataset. Initial cross-match of Gaia DR3 and *AllWISE*, i.e., *gdr3wise* shown in the left panel, and the red clump candidates selected from this are shown in the right panel, i.e., *gdr3wise*[RC] for the region $|Z_{GC}| < 2$ kpc.

mass red giant stars burning helium in their convective core, during which stage they have a relatively narrow distribution in their absolute magnitude, and with their age distribution peaking between $1 \sim 2$ Gyr (Cannon 1970; Girardi 2016). Over the years, the RC has been used to map out various features of the disc, such as the Galactic bulge/bar (Ness et al. 2012; Wegg & Gerhard 2013), to studying the warp, flare and scale-parameters (López-Corredoira et al. 2002; Wang et al. 2020; Bovy et al. 2016; Uppal et al. 2024), to mapping the large-scale velocity field of the disc (Bovy et al. 2015; Khanna et al. 2019a; Gaia Collaboration et al. 2021).

With the *Gaia* survey we now have a dataset with homogeneous all-sky photometry and astrometry, which allows the selection of large samples of stellar tracers of similar type. In Gaia Collaboration et al. (2021), *Gaia* EDR3 and 2MASS were combined to construct a catalogue of RC-like stars to study the kinematics of the outer disc. This sample was limited to a narrow region about the Galactic anti-centre ($|l - 180^\circ| < 20^\circ$), where extinction is minimal, allowing deep coverage far into the outer disc. In this contribution, we extend this approach to the entire sky. However, having a large sample of distance tracers is not enough by itself, as the goal is to compare the predictions from a sensible model to the data. Whereas the model lives in a perfect universe, in that it is unaffected by observational effects, the data is limited by the magnitude limits of the surveys used, incompleteness in data coverage due to inhomogeneity in data sampling, and any quality cuts that one imposes when compiling the data from one or more catalogues. Thus, to properly model the Galaxy (or indeed any system), one needs to bring the ideal model to the data space, i.e., take into account the selection effects and, importantly, the extinction. This is illustrated well by Li & Binney (2022), who recently modelled the youngest component of the disc using OB-type stars and explored the effects of incorrect dust models.

This study was made in the context of the *GaiaUnlimited* project¹, which has provided tools to the community to build Selection Functions for various datasets based on *Gaia* (Rix et al. 2021; Cantat-Gaudin et al. 2023a; Castro-Ginard et al. 2023; Cantat-Gaudin et al. 2024). Here, we apply some of these tools to model the density profile of RC stars in the Galactic disc. The text is organised as follows: In section 2 we describe the scheme to select RC stars and derive distances, section 3 lays out the scheme for building the selection function and the galac-

tic models we fit, in section 4 we present the results of the density modelling on both mock and observed data, and discuss these in detail in section 5.

2. Data

Our primary dataset is the official cross-match between *Gaia* DR3 and *AllWISE*, obtained from the *all_wise_best_neighbour* table provided on the *Gaia* data archive; the details of the cross-match algorithm are provided in Marrese et al. (2019)². We retain only those sources with finite measurement for parallax (ϖ), as well as photometry in both *Gaia* (G) and *AllWISE* (W_1 and W_2) bands. This gives a count of $N = 303,183,850$ sources. The all-sky distribution of this dataset, which we call *gdr3wise*, is shown in Figure 1 (left panel). Our algorithm to select RC stars is agnostic to the data quality; hence, at this stage we do not filter out poor data.

2.1. Photo-astrometric selection of the Red Clump

For each star, one can in principle compute the absolute magnitude (M_λ) in both the *AllWISE* ($\lambda = W_1$) and *Gaia* ($\lambda = G$) passbands as,

$$M_\lambda = m_\lambda - A_\lambda - \mu, \quad (1)$$

where $\mu = 5 \log_{10}(100/\varpi'[\text{mas}])$ is the distance modulus, and A_λ is the extinction in the passband λ , whose estimation is described in the following section. We adopt $\varpi' = \varpi + 0.017$ assuming a global parallax offset from Lindegren et al. (2021). However, applying Equation 1 would mean inverting the parallax to obtain an estimate for the distance modulus, which would yield problematic distances for sources with high parallax uncertainty, $\sigma_\varpi/\varpi > 0.2$ (Bailer-Jones 2015; Luri et al. 2018). In this light, we make use of the Bayesian distances estimated by Bailer-Jones et al. (2021)[hereafter *CBJ21*]. Their catalogue provides geometric distances (d_{geo}) for 1.47 billion sources, requiring only the *Gaia* EDR3 parallaxes. Additionally, for a large majority, they also provide photo-geometric distances (d_{photgeo}) for sources where G magnitude and $G_{\text{BP}} - G_{\text{RP}}$ colour are also available. In general, the *photogeo* distances are considered better for sources with high σ_ϖ/ϖ . However, these have a dependence on the stellar population modelling in the *Gaia* EDR3 mock catalogue (Rybizki et al. 2020) used as a prior, and could have complex behaviour at low latitudes, as noted by *CBJ21*. In any case, both

¹ <https://gaia-unlimited.org/>

² Gaia crossmatch documentation

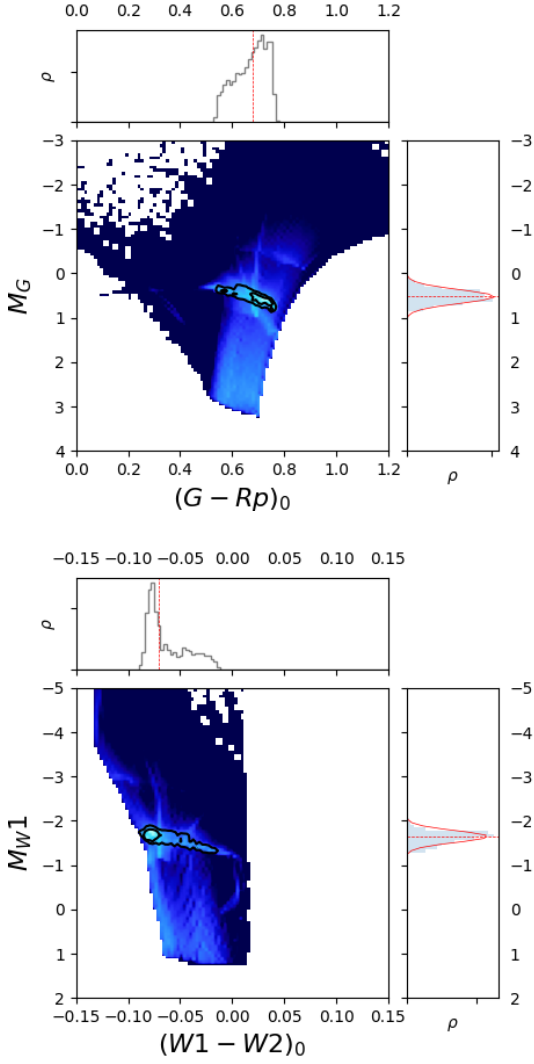


Fig. 2. Distribution of giants on the *CaMD* diagram, in a mock realisation of the Milky Way using the *Galaxia* code (see subsection B.2). The top panel shows M_G vs. *Gaia* colours, while the bottom panel shows M_{W1} vs. *AllWISE* colours. The RC is marked by the black contours. The marginalised histogram (normalised) for the x (top subpanel) and y (right subpanel) axes are also shown. For the RC, both M_G and M_{W1} can be approximated by a quasi-Gaussian as is shown by the red curves on the right insets.

distance estimators are dependent on the assumed 3D density distribution of stars in the Milky Way, and in the case of *CBJ21* this is derived from the Besançon Galactic model (Robin et al. 2003a) used to construct the *Gaia* EDR3 mock catalogue of Rybizki et al. (2020). Following *CBJ21*, we construct the posterior probability distribution function (PDF hereafter) of distances (d) for every source in our sample. This can only be done for their geometric distances, and in any case our intention here is to use an informed prior with as few assumptions as possible, and only for the purpose of selecting RC candidates. We use the distance priors and a likelihood function (see Appendix A), to compute the PDF on a grid of 500 points (d_1, d_2, \dots, d_n), with $d_1 = 0$, and $d_n = 2 \times (d_{\text{photgeo}}/d_{\text{geo}})$, i.e., setting the maximum grid point to be twice the distance prior for each source. In general, we use d_{photgeo} distances where available, but for the minority of sources that don't have these provided, we use d_{geo} distances instead. We use the median value of the distance PDF, along with sky po-

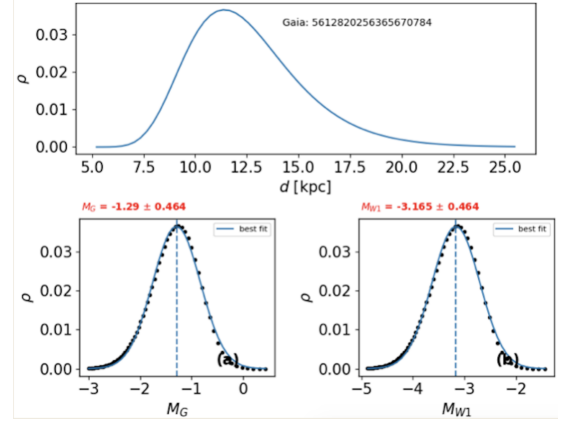


Fig. 3. Procedure to obtain the distribution of the absolute magnitude starting from distance priors illustrated for two example sources. For each example, the top inset shows the distance prior used, which is turned into a grid of absolute magnitude using 3D extinction maps. The bottom figures show a Gaussian fit to the resulting absolute magnitude distributions in the *G* and *W1* bands used to select the RC candidates.

Table 1. Median absolute magnitude \bar{M}_λ , and dispersion in absolute magnitude $\sigma_{\bar{M}_\lambda}$ for typical RC stars, as listed in Hawkins et al. (2017).

| Passband (λ) | \bar{M}_λ | $\sigma_{\bar{M}_\lambda}$ |
|------------------------|-------------------|----------------------------|
| <i>W1</i> | -1.68 ± 0.01 | 0.10 ± 0.02 |
| <i>G</i> | $+0.44 \pm 0.01$ | 0.20 ± 0.02 |

sition (l, b) to estimate the reddening $E(B - V)$, and using the reddening coefficients listed in subsection 2.3 to convert to extinction A_λ . We then convert the distance grid to that in absolute magnitude, (i.e., $M_{\lambda,1}, M_{\lambda,2}, \dots, M_{\lambda,n}$), thus obtaining the posterior PDF in M_λ , to which we fit a broad *Gaussian* (\mathcal{N}) profile in order to obtain the peak and spread (σ_{M_λ}) in the inferred distribution. Since any given star has single true absolute magnitude, σ_{M_λ} quantifies our uncertainty on our inferred M_λ value, taken as the mean of the fitted Gaussian, due to distance and extinction uncertainties. This procedure is illustrated in Figure 3.

The absolute magnitude for the RC has been calibrated in several passbands, for example by Hawkins et al. (2017) and Ruiz-Dern et al. (2018), who also considered variations due to colour. Khanna et al. (2019a, K19 hereafter) calibrated the absolute magnitude in the *K* band as a function of metallicity $M_K([\text{Fe}/\text{H}])$ using the *Galaxia* code (Sharma et al. 2011). They showed that the dependence of M_K on metallicity is non-negligible for stars with $[\text{Fe}/\text{H}] < -0.4$ dex, while beyond this metallicity, the M_K is roughly flat with $[\text{Fe}/\text{H}]$ (see their Figure A.4). How many $[\text{Fe}/\text{H}] < -0.4$ RC stars we expect to observe depends on the age distribution, and the apparent magnitude limit of the sample. In subsection B.2, we select RC stars from a Milky Way analogue generated using *Galaxia*. For these, Figure 2 shows the distribution of M_G vs. $(G - R_p)_0$, and M_{W1} vs. $(W1 - W2)_0$, with the locus of the RC marked by black contours. Figure B.4 shows the cumulative distribution function (CDF) of metallicity for the RC. We show the CDF profile for three different age caps, that is assuming the maximum age of the RC sample in the Galactic disc is $\tau = (5, 7, 10)$ Gyr. We find that the expected fraction of RC at $[\text{Fe}/\text{H}] < -0.4$ is about 12 % for a cap of $\tau < 7$ Gyr, and reaches about 20% for $\tau < 10$ Gyr. Since the age distribution of RC generally peaks around 1 ~ 2 Gyr (Girardi 2016), we do not expect many RC stars at $[\text{Fe}/\text{H}] < -0.4$ dex, and will thus neglect this small metallicity dependence in the ab-

solute magnitude. Table 1 lists the absolute magnitude (\bar{M}_λ) and intrinsic dispersion $\sigma_{\bar{M}_\lambda}$ for the RC, in the photometric bands used here, according to Hawkins et al. (2017).

In order to select the RC we assume that the distribution in absolute magnitude space is a 2D Gaussian with the centroid at $(\bar{M}_G, \bar{M}_{W1})$. In general for a given distribution, the distance between its centroid (x_0) and a point of interest (x_1) can be given in terms of the Mahalanobis distance (ML), given as

$$ML^2 = (x_1 - x_0)^T \Sigma^{-1} (x_1 - x_0), \quad (2)$$

that respects the combined covariance (Σ) of x_0 and x_1 . In our context, x_0 and x_1 are the two dimensional mean absolute magnitudes of the RC and of our inferred absolute magnitudes (M_G, M_{W1}). The covariance is then given as

$$\Sigma = \begin{pmatrix} \sigma_{M_G}^2 + \sigma_{\bar{M}_G}^2 & 0 \\ 0 & \sigma_{M_{W1}}^2 + \sigma_{\bar{M}_{W1}}^2 \end{pmatrix} \quad (3)$$

where the diagonal terms combine the spread in the observed (σ_{M_λ}) and true dispersion of absolute magnitudes ($\sigma_{\bar{M}_\lambda}$), and we assume the off-diagonal elements of Σ are 0, that is, that the photometric uncertainties of the *Gaia* and *AllWISE* surveys are uncorrelated. Essentially, ML is a measure of the distance from the centroid in units of the standard deviation. Assuming the underlying distribution is multinormal (in M_G, M_{W1}) we can define a p-value, that is the probability of finding a value of ML^2 or greater under the null-hypothesis of the star not being part of the RC, from a chi-square distribution. We select those stars for which the probability is greater than the p-value. In practice we choose to select all those stars that fall for inside the $3\text{-}\sigma$ contour for a 2D Gaussian,

$$\chi^2(ML^2, \dim = 2) < \chi^2(3^2, \dim = 2) \quad (4)$$

Using the procedure above for each star in the *gdr3wise* dataset we find a total number of 9,761,294 RC stars, and will refer to it as *gdr3wise*[RC]. See Figure 1 for the distribution of the RC stars over the whole sky. We note that there is a faint offshoot from the bulge at about $l = 5$ deg which are likely contaminants from the Sagittarius stream, but we will be excluding data within $R < 3$ kpc when modelling the disk distribution in later sections.

2.2. Coordinate system

Our adopted coordinate system is illustrated in Figure 4. We first transform our (l, b) and distance d coordinates to heliocentric Cartesian coordinates, with the X -axis pointing toward the Galactic Center:

$$\begin{pmatrix} X_{\text{hc}} \\ Y_{\text{hc}} \\ Z_{\text{hc}} \end{pmatrix} = d \begin{pmatrix} \cos b \cos l \\ \cos b \sin l \\ \sin b \end{pmatrix}, \quad (5)$$

To transform these heliocentric coordinates to Galactocentric Cartesian coordinates we assume $R_\odot = 8277 \pm 9(\text{stat}) \pm 30(\text{sys})$ pc from the ESO Gravity project's most recent measurement of the orbit of the star S2 around the the Milky Way's supermassive black hole (Gravity Collaboration et al. 2021). The heliocentric Cartesian frame is then related to Galactocentric one by a simple translation: $X_{\text{hc}} = X_{\text{GC}} + R_\odot$, $Y_{\text{hc}} = Y_{\text{GC}}$ and $Z_{\text{hc}} = Z_{\text{GC}} - Z_\odot$. The galactocentric cylindrical radius R is trivially found from $\sqrt{X_{\text{GC}}^2 + Y_{\text{GC}}^2}$, while the cylindrical coordinate angle

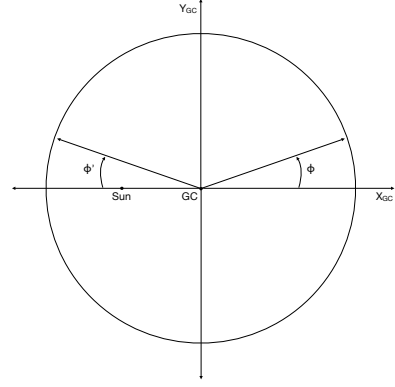


Fig. 4. Coordinate system adopted in this paper.

$\phi = \tan^{-1}(Y_{\text{GC}}/X_{\text{GC}})$ increases in the anti-clockwise direction, while the rotation of the Galaxy is clockwise, as seen from the north. The height of the Sun above the Galactic plane is adopted as $Z_\odot = 0$ pc (Gaia Collaboration et al. 2023, hereafter Gaia23), though we found that our results remain unchanged even when we used the alternative $Z_\odot = 27$ pc (Bennett & Bovy 2019). The uncertainties in our transformed coordinates are dominated by the uncertainties in distance estimates. We do not propagate these through the coordinate transformation, but instead generate multiple realisations of the data, each time sampling distances from the underlying distribution (see subsection 2.4).

2.3. 3D Extinction maps

In order to compute the absolute magnitude, we need good estimates of the extinction A_λ in passband λ . The widely used maps of reddening, $E(B - V)$, from Schlegel et al. (1998, hereafter S98), estimates the extinction at infinity given a star's 2D (l, b) sky coordinates. While these dust maps cover the entire sky, the 2D extinction values will overestimate the reddening for sources that are not outside the ISM layer. This can be improved upon by using 3D dust maps that require a prior for distances. All stars in our sample have a measured parallax, so in principle one could use this as a prior to estimate the distance, but as discussed earlier, instead we make use of the distances from *CBJ21*, as our purpose here is only to use these initial distance estimates to arrive at a realistic first-estimate of the foreground extinction along a given line-of-sight. For the selected sample of RC stars, we will derive distances independently, as described in subsection 2.4.

At the time of running our algorithm, we had access to the following publicly available 3D dust maps: a) The Lallement et al. (2019) map³, derived with *Gaia* and 2MASS photometry and *Gaia* astrometry. This map provides the *Gaia* extinction parameter A_0 , defined as the monochromatic extinction at 541.4nm, at a resolution of 5 parsecs within 3 kpc from the Sun and within 0.5 kpc perpendicular to the plane. b) Further out, we make use of the *Bayestar* 3D extinction map by Green et al. (2019). This is based on a Bayesian scheme, combining *Gaia* DR2 parallax with photometry from 2MASS and *Pan-STARRS* surveys. The spatial coverage is limited to the sky north of declination (dec) of -30° . For each source, we multiply the *Bayestar* map output by a multiplicative factor to obtain the reddening, i.e., $E(B - V) = 0.884 \times E(\text{Bayestar}19)$, as recommended⁴. c) For the remainder of the sky, we return to the S98 map, but in order to correct for the overestimation in the extinc-

³ https://astro.acri-st.fr/gaia_dev/about

⁴ <http://argonaut.skymaps.info/usage>

Table 2. Parameters for the dust model adopted in this paper, with values taken from Robin et al. (2003b) .

| Parameter | Value | Unit |
|-----------------|-----------------|-------------------|
| h_R | 4.2 | kpc |
| h_z | 0.088 | kpc |
| γ_{fl} | 0.0054 | kpc ⁻¹ |
| γ_{warp} | 0.18 | kpc ⁻¹ |
| R_{fl} | 1.12* R_\odot | kpc |
| R_{warp} | 8.4 | kpc |

tion, we estimate a dust fraction factor (following Koppelman & Helmi (2021)), as:

$$\frac{E_{B-V}(l, b, s)}{E_{B-V, \infty}(l, b)} = \frac{\int_0^s \rho[x(s')] ds'}{\int_0^\infty \rho[x(s')] ds'}, \quad (6)$$

where $E_{B-V, \infty}(l, b)$ is the extinction estimate from S98, s is the heliocentric distance to a source, and x is the position vector. $\rho(R, z)$ is the dust density model, we adopt, in this case from Sharma et al. (2011),

$$\rho(R, z) \propto \exp\left(\frac{R_\odot - R}{h_R} - \frac{|z - z_{warp}|}{k_{fl} h_z}\right), \quad (7)$$

with the disc warping, and flaring (fl) modelled as,

$$\begin{aligned} k_{fl}(R) &= 1 + \gamma_{fl} \text{Max}(0, R - R_{fl}) \\ z_{warp}(R, \phi) &= \gamma_{warp} \text{Max}(0, R - R_{warp}) \sin(\phi). \end{aligned} \quad (8)$$

The parameters of the model are taken from Robin et al. (2003b), and are listed in Table 2. In the *AllWISE* bands, we adopt the following reddening coefficients: $A_{W1}/E_{(B-V)} = 0.174$, and $A_{W2}/E_{(B-V)} = 0.107$ (Sharma et al. 2011). Using the *dustaprox* code, we apply the mid-IR extinction curve from Gordon et al. (2023) and adopting $R(V) = 3.1$ to compute the ratios, $A_{W1}/A_G = 0.07$, $A_{W1}/A_{Bp} = 0.05$, and $A_{W1}/A_{Rp} = 0.09$, appropriate for a typical red clump star ($4200 < T_{\text{eff}} < 5400$ K, $1.8 < \log g < 3.2$). We find that these ratios are insensitive to $[\text{Fe}/\text{H}]$.

2.4. Red clump distance and uncertainty

For every star classified as RC and assumed as having an absolute magnitude M_λ as per table 1, we can invert Equation 1 to calculate the distance modulus, but since the extinction A_λ itself depends on the distance, we follow an iterative procedure instead. First, we derive the maximum possible distance modulus for a star, assuming zero extinction along the line-of-sight,

$$\mu_{\text{max}i} = m_\lambda - M_\lambda \quad (9)$$

using this, we can in turn derive the maximum distance (d_{max}) and then compute the extinction, $A_\lambda(l, b, d_{\text{max}})_i$, to in turn compute an updated distance modulus,

$$\mu_i = m_\lambda - M_\lambda - A_\lambda(l, b, d)_i. \quad (10)$$

Using μ_i we then recompute $A_\lambda(l, b, d)_i$, and repeat the procedure until the distance modulus is converged (typically within 5 iterations) to $\bar{\mu}_\lambda$. For every star we sample the absolute magnitude from a *Gaussian* $\mathcal{N}(\bar{M}_\lambda, \sigma_{\bar{M}_\lambda})$, using the values listed in Table 1, to derive the PDF of the distance modulus.

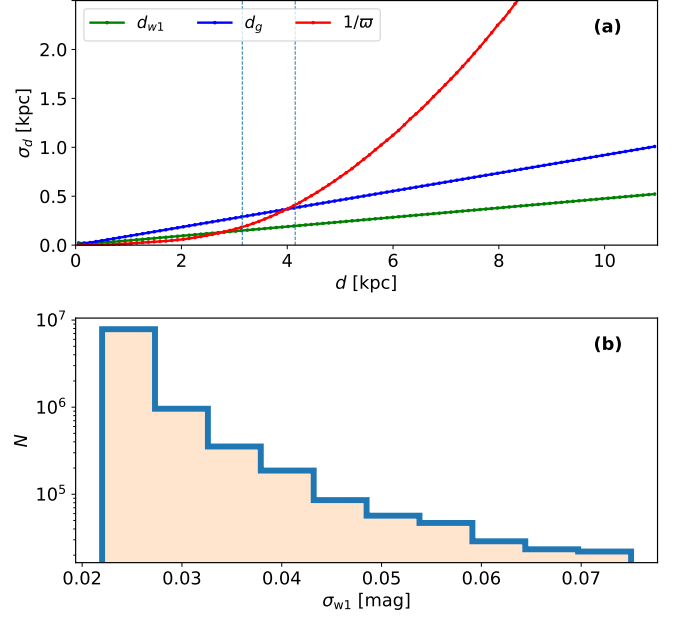


Fig. 5. Panel (a): Typical distance uncertainty for the red clump as a function of distance. The red curve shows the expectation from a naive inverse parallax estimation, the blue curve shows the predicted uncertainties in the photometric distances in *G* band and for *W1* this is shown by the green curve. The two vertical dotted lines indicate roughly the distances beyond which the photometric distances become more informative than parallax inversion for the two bands. Panel (b): Distribution of photometric uncertainty in *W1* for the RC stars shows that $\sigma_{W1} \ll 0.1$ i.e., lower than the intrinsic dispersion in the absolute magnitude of RC stars in *W1*.

From Equation 9, we can consider two main sources of uncertainty in our distance estimate, a) $\sigma_{\bar{M}_\lambda}$: The intrinsic dispersion in the absolute magnitude, and b) σ_{m_λ} : The photometric uncertainty. From Table 1 we see that $\sigma_{\bar{M}_\lambda}$ is twice as large in the *G* band (0.2mag) compared to that in *W1* (0.1mag). For this reason, we decided to use only the distances based on *W1* passband, in order to minimise the distance uncertainty and the effects of extinction. As for photometric uncertainty, we find that about 99.5% of our RC sample has $\sigma_{W1} < 0.1$. In fact Figure 5(b) shows that the overall $\sigma_{W1} \ll 0.1$, i.e., the photometric uncertainties are generally much smaller compared to the intrinsic dispersion in the absolute magnitude in *W1*. We exclude the remaining 0.5% of the sources that have $\sigma_{W1} > 0.1$, though given their insignificant number, their removal or not makes no noticeable difference in the results. For every star, we combine the two sources of uncertainty in quadrature to derive the uncertainty in the distance modulus as

$$\sigma_{\mu(W1)} = \sqrt{\sigma_{m_{W1}}^2 + \sigma_{\bar{M}_{W1}}^2}. \quad (11)$$

Strictly, one should also consider the uncertainties in the extinction maps, but since in this contribution we use a combination of various maps, this is not a trivial exercise, and we ignore it for simplicity. However, since we use primarily the distances based on *W1*, we anticipate this to be a small effect. We assume the uncertainties in the distance modulus are *Gaussian*, i.e., $\mathcal{N}(\bar{\mu}_\lambda, \sigma_{\mu(W1)})$. It can be shown then that the typical uncertainty in the photometric distance (d) is, $\sigma_{d_{RC,\lambda}} = 0.2 \ln(10) \sigma_{\mu_\lambda} d$, while a naive inversion of the parallax results in distance error given by $\sigma_{d_\varpi} = \sigma_\varpi d^2$, where σ_ϖ is the parallax error. Figure 5(a) compares the profiles of the distance uncertainty with respect to

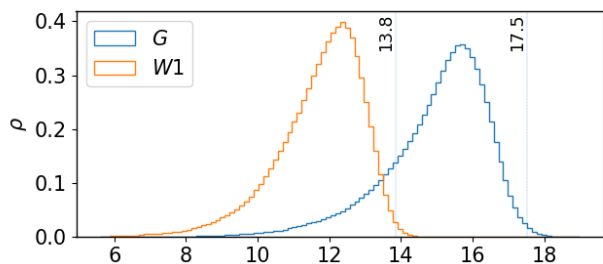


Fig. 6. The apparent magnitude distribution of the *gdr3wise*[RC] sample, in the *G* and *W1* bands. The vertical dashed lines at $G=17.5$ and $W1=13.8$ indicate the 99.5th percentiles in the respective bands.

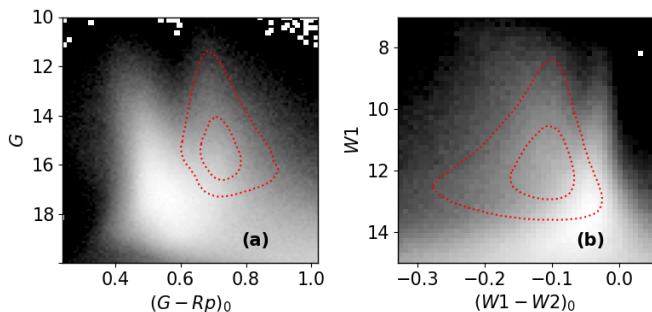


Fig. 7. colour Magnitude diagram for the *gdr3wise* parent catalogue shown in gray for *Gaia* and *AllWISE* colours. In each panel, we indicate the selected RC sample using the red contours (1σ , 2σ).

distance from the two approaches, showing that beyond a heliocentric distance of about 3 kpc, the RC distances are superior.

2.5. RC catalogue and validation

In Figure 1, we show the full sky distribution (l, b) at healpix level 5, for the *gdr3wise* crossmatch (left panel), and for the selected RC candidates (right panel). The apparent magnitude distribution of the selected RC sample is shown in Figure 6, where we note the faint limits (99.5 percentile) being at $m_{G,lim}=17.5$, and $m_{W1,lim}=13.8$. We note that *AllWISE* is essentially complete in this magnitude range (Schlafly et al. 2019, see their Figure 4). We show in Figure 7, the colour-magnitude distribution (grey) for the *gdr3wise* parent sample in both *Gaia* and *AllWISE* colours. In each panel, the bifurcation between Giants and dwarfs is apparent, and indicated in red contours is the region occupied by our selected RC sample.

Most of the selected sources are confined within $|b| < 10^\circ$ of the plane, but our algorithm also picked out sources around the Large (LMC) and the Small (SMC) Magellanic clouds. The LMC ($RA, DEC = 81.28, -69.78$) is known to be at a distance of about 50 kpc from the Sun (Pietrzyński et al. 2019). Along this line of sight, we estimate extinction of $A_{W1} = 0.15$, and $A_G = 2.38$. From Equation 1, we would then expect the brightest RC in the LMC to be visible at $G = 21.3$ or $W1 = 16.9$, which lie outside the magnitude distribution of our RC candidates. Instead, these sources enter the selection because the *CBJ21* catalogue has no priors for LMC/SMC stars, and since the relative parallax uncertainty is high for these sources, they are assigned incorrect distances. Our goal is to primarily select RC stars in the Milky Way disc, so for density modelling, we restrict our final sample to the region $|Z_{GC}| < 2$ kpc which also removes the contamination

at $b > -30^\circ$ from the Magellanic clouds, as in Figure 1. Though we note that the results remain changed even without this cut, because of the very low relative contamination from these stars to the total number of about 10 million.

In Figure 8(a) we show the density maps for this dataset, in the Galactocentric $X_{GC}-Y_{GC}$ projection, showing clearly the region in the inner Galaxy ($R < 3$ kpc) that we mask. Our sample provides a good coverage between $3 < R < 14$ kpc. Figure 8(b) shows the corresponding $Y_{GC}-Z_{GC}$ projection to show the extent of the coverage vertically w.r.t the midplane of the disc. This is also illustrated in Figure 9, where it is clear that most of the sample lies within $|Z_{GC}| < 1.5$ kpc, and that towards the outer disc ($R > 10$ kpc) there is a hint of flaring in the vertical counts. To see this more clearly, in Figure 10(a) we plot the number counts as a function of Z_{GC} at successive R annuli, spanning from 3 to 17 kpc. The slope of the profiles is a measure of the scale-height of the disc at a particular annulus, while a change in the slope from the inner to the outer disc would indicate a change in the scale-height, thus flaring if the scale-height increases with R . Figure 10(b) shows the vertical number counts folded along the Z_{GC} axis (i.e. $|Z_{GC}|$), which makes it easier to spot the changing slope with R , in particular beyond $R = 11$ kpc. We remind the reader, however, that Figure 10 shows the vertical counts in the data without accounting for the selection function, therefore fitting a model (for example an exponential) directly to this figure is not appropriate. Here we are simply presenting the data for a visual inspection, and note the hints of a flared disc.

Any scheme for the selection of the RC based purely on astrometry and photometry is bound to have contamination from neighbouring populations. This is mainly due to limitations such as the quality of extinction maps, and uncertainty in photometry and parallax. Also, in the case of the RC, intrinsic colour and magnitude are not enough to separate such stars from Red giant branch (RGB) stars occupying the same part of the HRD. In such cases, however, while not true RC stars, their true photometric distances will not be too different than those of the true RC. Since we are able to select a very large sample of RC candidates, we carry out a comparison with a few spectroscopic (*GALAH* and *APOGEE*), and asteroseismic catalogues for validation in Appendix B. For the stars that are found in common with these catalogues, we find that their distribution in the *Kiel* (Figure B.3), colour-magnitude (Figure B.1), and colour-absolute-magnitude diagrams (Figure B.2, is reasonable for our RC sample.

3. Method

3.1. Modelling the Galactic disc

The number density distribution, $N(R, z)$, in our model is described by two exponential discs, each of the form,

$$N(R, z) \propto \exp\left(-\frac{R}{R_d} - \frac{R_{cut}}{R} - \frac{|z - z_w|}{h_z}\right), \quad (12)$$

with scaleheight (h_z), scale-length (R_d), and an inner-cut radius (R_{cut}), which excludes the region not described by the disc, such as in the inner Galaxy (Aumer & Binney 2017; Vasiliev 2018). The disc is exponentially flared, i.e., h_z increases with R , controlled by the flare scale-length, R_{fl} ,

$$h_z = h_{z,\odot} * \exp\left(\frac{R - R_\odot}{R_{fl}}\right), \quad (13)$$

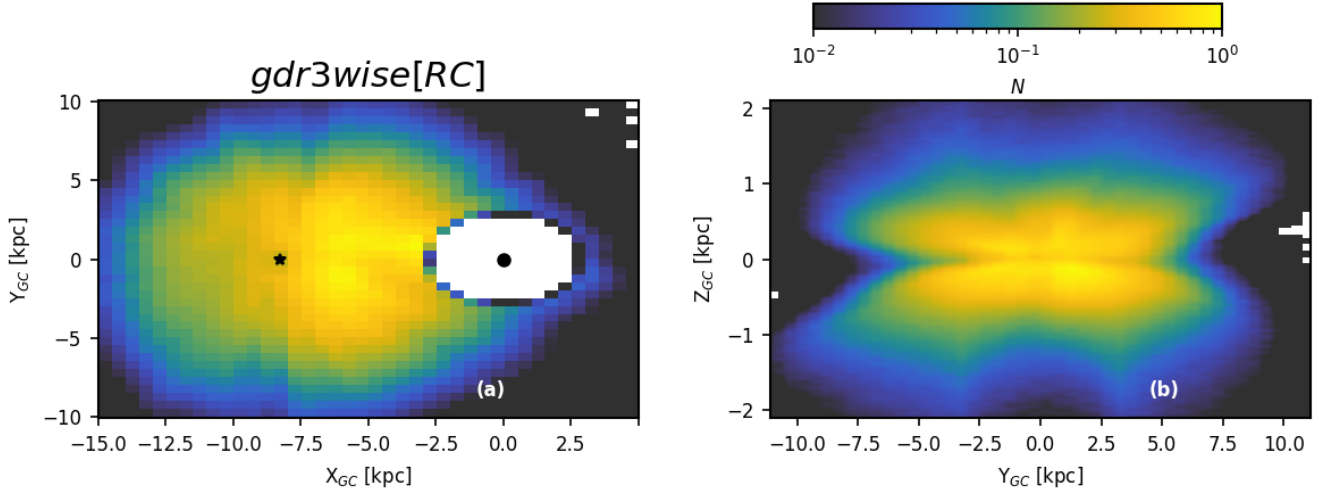


Fig. 8. Spatial distribution of the *gdr3wise*[RC] sample, for the region considered for model fitting. Panel (a) shows the Galactocentric X_{GC} - Y_{GC} projection, with the location of the Sun (black star), and the Galactic centre (black dot) also indicated. Stars within $R < 3 \text{ kpc}$ of the Galactic centre have been removed. Panel (b) shows the corresponding Galactocentric Y_{GC} - Z_{GC} projection. The number density is shown on a logarithmic scale.

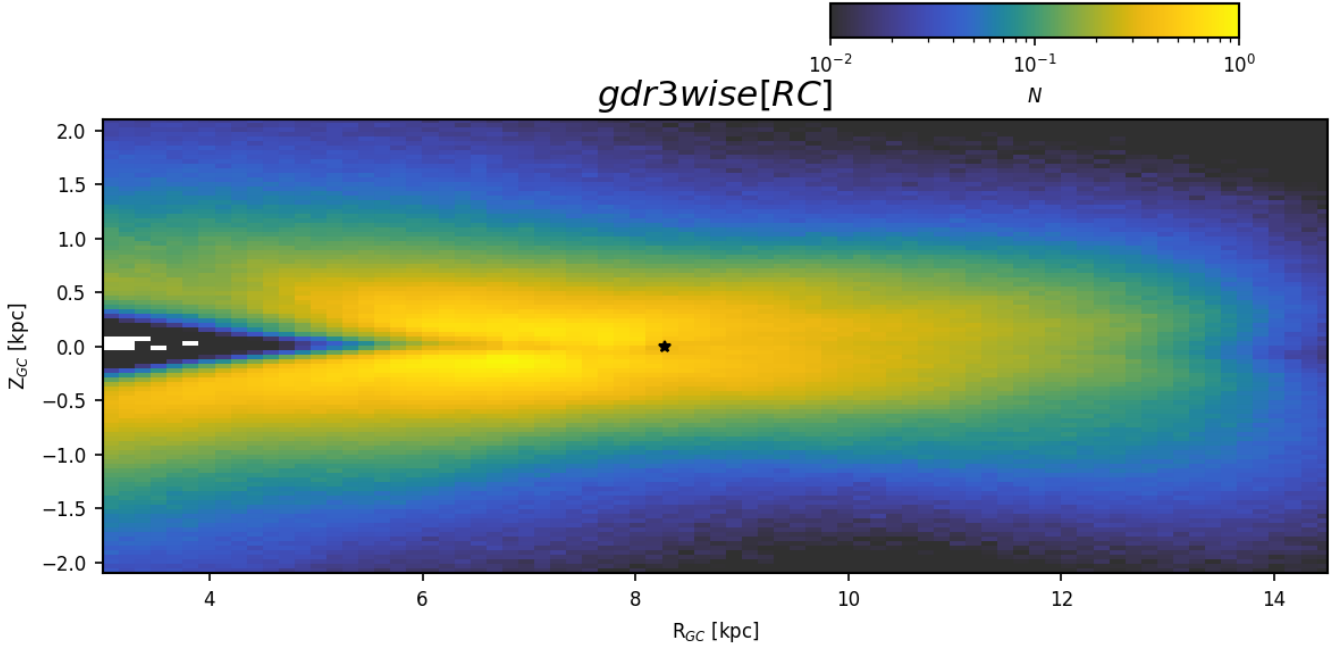


Fig. 9. Galactocentric R - Z_{GC} projection for the *gdr3wise*[RC] sample, over the region that is considered for our model fitting. The number density is shown on a logarithmic scale. The location of the Sun is indicated as a black star.

with scale-height normalisation $h_{z,\odot}$ at the solar radius R_{\odot} . The total density is thus given by,

$$N(R, z) \propto f_{d1} \times N(R, z)_1 + (1 - f_{d1}) \times N(R, z)_2 \quad (14)$$

with f_{d1} being the mass contribution of the first disc. The density function is normalised such that over the observed volume $\int_V F \times N(R, z) dV = N_{\text{observed}}$, where the fraction of observable stars ranges between $F = [0, 1]$ (see subsection 3.2). We also consider a warped disc in one of the components. This is parameterised as,

$$z_w = h_w \times (R - R_w)^{a_w} \sin(\phi' - \phi_w), \quad (15)$$

where the onset of the warp is at R_w (i.e., $z_w = 0$ inside this radius), and its amplitude is set by h_{w0} . The warp is sinusoidal such

that the line of nodes lies along $\phi' = \phi_w$, where, $\phi' = \tan^{-1} \left(\frac{Y_{GC}}{-X_{GC}} \right)$, being zero toward the anticenter and increasing in the direction of Galactic rotation. We distinguish this from the galactic azimuth, $\phi = \tan^{-1}(Y_{GC}/X_{GC})$, which instead increases anti-clockwise (see Figure 4). We do so to both be consistent with standard coordinate frame conventions, as well as those preferred by the warp modelling papers.

The Milky Way is known to host a bar, and over the past several years, the range of the bar length ($3 < R_b < 5 \text{ kpc}$) has been estimated using various tracers (Gaia23 and references within). For our purpose we would like to retain as much of the disc region as possible while removing the probable regions most affected due to the central bar. Recently, Vislosky et al. (2024) estimated a value of $R_b = 3.6 \text{ kpc}$, but suggest that it could be as

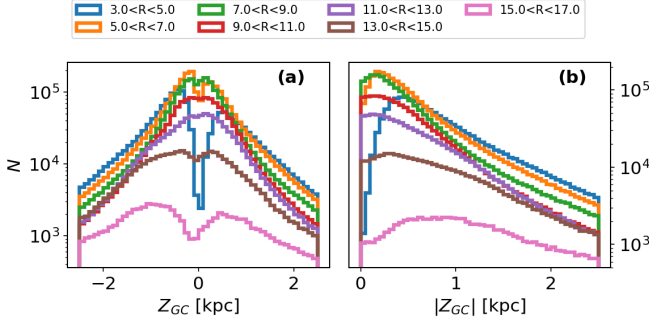


Fig. 10. Vertical counts of *gdr3wise*[RC] for successive annuli in R between 3 to 15 kpc. Panel(a) shows the counts as a function of Z_{GC} , while panel(b) shows the same folded along the vertical axis i.e., $|Z_{GC}|$. In panel(b) a change of slope in the vertical counts is evident as we move from the inner to the outer disc region.

Table 3. Parameters to be fitted and the range of values allowed. The first set of parameters describe the structure of the disc, such as the scale-length, scale-height and flare. The four parameters that describe the warp are listed separately at the bottom.

| Parameter | Range | Description |
|--------------------------------|----------------|---|
| R_d | [1, 5] kpc | Scale-length of disc 1. |
| $h_{z,\odot}$ | [0.1, 1.5] kpc | Scale-height of disc 1 at R_\odot . |
| $\log_{10} R_{fl}$ | [-3, 3] | Logarithm of flare scale-length (kpc) for disc 1. |
| f_{d1} | [0.05, 1.] | Mass fraction of disc 1. |
| R_{d2} | [1, 5] kpc | Scale-length of disc 2. |
| $h_{z,\odot}$ | [0.1, 1.5] kpc | Scale-height of disc 2 at R_\odot . |
| Warp Parameters (disc 1 only): | | |
| ϕ_w | [90°, 270°] | ϕ' of the line of nodes. |
| R_w | [1, 15] kpc | radial onset of the warp. |
| a_w | [0, 5] | radial exponent of the warp. |
| h_{w0} | [0, 5] kpc | amplitude of the warp. |

low as 3 kpc. For this reason, we fix the inner-cut radius, $R_{cut} = 3$ kpc. Our tests showed that increasing R_{cut} to 3.5 kpc barely impacted the results, so we chose to stick to the lower bound of R_b . For our RC sample, the ϕ – R projection is shown in Figure 11. Our full model fits for a maximum of 10 parameters. These are the scale parameters of the first disc (R_d , $h_{z,\odot}$, R_{fl}), and its mass fraction (f_{d1}), and four parameters describing the warp (ϕ_w , R_w , a_w , h_{w0}), and the scale parameters of the second disc (R_{d2} , $h_{z,\odot}$). We only allow the first disc to be warped and flared. Our initial exploration of the observational data showed no major difference if both disc components were allowed to be both flared and warped, so in order to reduce the parameter space and degeneracy between parameters, we imposed this condition. All the parameters we fit for are listed in Table 3, along with their bounds and units.

3.2. Selection Function

We now discuss the various layers of the selection function that need to be accounted for in our modelling of the observational data. If we consider stars in a 3D grid in space, in this case, in $X_{GC} \times Y_{GC} \times Z_{GC}$, our goal is to be able to predict the number counts in each voxel i .

$$N_i = N_{i,true} \times S_i \quad (16)$$

where $S_i[0, 1]$ is the correction factor (selection function) to the counts predicted by the model, $N_{i,true}$. In the ideal case S_i would

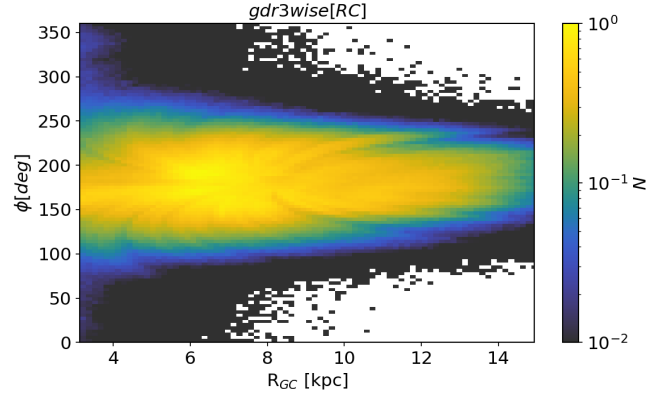


Fig. 11. Spatial distribution in the ϕ – R projection of the observational red clump sample, constructed from the *gdr3wise* parent dataset. The range shown here is the region over which we perform our model fitting.

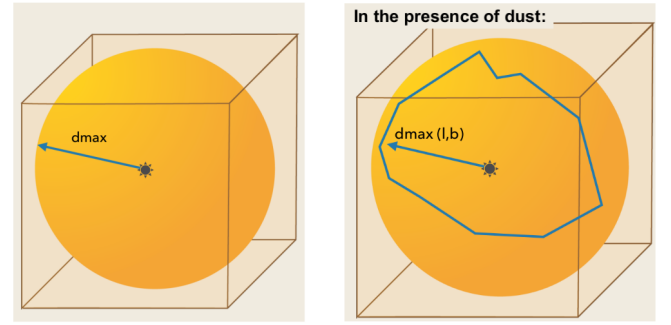


Fig. 12. Cartoon illustrating the maximum observable distance (d_{max}) for the RC, for a magnitude limited survey. The left panel shows the ideal situation when there is no dust extinction, in which case the observable region traces out a sphere with radius d_{max} . On the right, is shown the case with extinction which depends on sky position (l, b), due to which $d_{max}(l, b)$ varies across the sky, modifying the effective volume from that of a perfect sphere.

be equal to 1, if we are able to observe the entire ground truth, that is, all stars of our modelled population in a given voxel i , and in the worst case would be 0, if there was missing or poor quality data in some patches of the sky, but also if the survey isn't designed to observe certain fields. In our specific case, S_i is the fraction of the RC stars in voxel i that can be seen for our sample. However, we point out that in general the selection function is dependent on observable quantities (Rix & Bovy 2013; Frankel et al. 2020), and here we can only define an S_i for a given voxel i and interpret it as the fraction of stars in that voxel because we are dealing with a standard candle, allowing us to translate the observed apparent magnitude into a distance, once we assume an extinction map. We can set out two principle layers that determine S_i :

a.) Effective volume: For a magnitude limited survey, ($m_\lambda < m_{\lambda,lim}$), for a quasi-fixed absolute magnitude, such as is the case with the RC, we can define a maximum distance modulus (μ),

$$\mu_{max} = m_{\lambda,lim} - M_\lambda, \quad (17)$$

such that from our position at the Sun, the observable volume would be traced out by a sphere with a radius (d_{max}) equal corresponding to this maximum distance modulus. However, here we have neglected the presence of interstellar dust, which is an

unavoidable evil in the Galaxy, accounting for which the maximum distance modulus μ_{max} is now no longer a constant, but instead varies for each voxel i :

$$\mu_{max,i} = m_{\lambda,lim} - M_{\lambda} - A_{\lambda}(l, b, d)_i, \quad (18)$$

Consequently, the observable or effective volume is crumpled and no longer a simple sphere, as illustrated in Figure 12. Essentially, this is similar to integrating a density function over the whole sky, but with the limits on distance varying by line-of-sight. Hence, depending on the dust distribution, the limit of the volume sampled varies in different directions on the sky. Along some lines-of-sight one can only map to a few kpc, while along others it is possible to map out the edge of the Galactic disc. Thus we need to take into account this dust/ $m_{\lambda,lim}$ induced distance limit.

Since we are modelling the number counts on a fixed 3D grid, we must also take into account the finite size of our voxels. We can pre-compute the fractional effective volume, F_i , for each volume element (ie. voxel), and then apply it to both simulated and observational data. For example, let us consider a cube shaped grid ($X_{GC} \times Y_{GC} \times Z_{GC}$), where every voxel has the same size, and is small enough such that the median heliocentric distance of all stars in that voxel can be approximated by the median heliocentric distance of that voxel. Then for every voxel (l, b, d_i) we can check if $d_i < d_{max}(l, b)$ (d_{max} condition), and retain only those that satisfy this condition. However, for nearby voxels the size of the voxel may be significant with respect to its heliocentric distance, or the extinction may vary significantly within a voxel. In this case the median quantities of the voxel (l_i, b_i, d_i) are not representative of the median quantities of the stars within it. This becomes more of an issue if the volume elements of the adopted grid do not have a fixed size. In this work, because the number of stars decrease exponentially with Galactocentric radius, to increase the statistical significance of the counts per voxel in the outer disk, we adopt a cylindrical grid (R, ϕ, Z_{GC}), so that the volume of the voxels increase with R , fixing the cylindrical grid to the binning ($\Delta R, \Delta \phi, \Delta Z_{GC}$) = (0.25 kpc, 10° , 0.25 kpc), from $R_{min}=3$ to 20 kpc in radius, 0 to 360° in ϕ , and between ± 2 kpc in Z_{GC} .

As an example let's first consider such a cylindrical grid where for every voxel we compute the heliocentric distance at its center. Then we assume a single absolute magnitude $M_G = 0.44$ for our RC stars, so that for a given magnitude limit (say $G = 16$), we can estimate the d_{max} . In Figure 13 we consider the case without extinction, so d_{max} is a constant (12.94 kpc), and at $Z_{GC}=0$ kpc, i.e., right in the midplane. Figure 13(a-c) show the ϕ vs. R projection of the voxels, mapped by different quantities. Figure 13(c) shows the projection mapped onto heliocentric distance, only for those voxels that satisfy $d_i < d_{max}$ (using the center of the voxel). So it follows that in Figure 13(b), all voxels outside of this condition have F_i set equal to 0, that is, no RC stars in this volume element will be in our magnitude limited sample, while those inside have F_i set equal to 1, i.e., the selection function resulting from the magnitude limit is binary, as expected.

To check if this approximation is valid, we sub-bin our 3D cylindrical grid by a factor of 5 in each dimension (125 subvoxels) and then in each voxel we can count the number of subvoxels that satisfy the d_{max} condition, to now obtain a fractional selection function ($N_{d<d_{max}}/125$ instead of a binary 0 or 1). Figure 13(a) shows the ϕ vs. R mapped in the midplane by this corrected selection, which we can now compare it to the previous simple binary selection in Figure 13(b). We can see that while for most voxels the correct selection function is identical to that

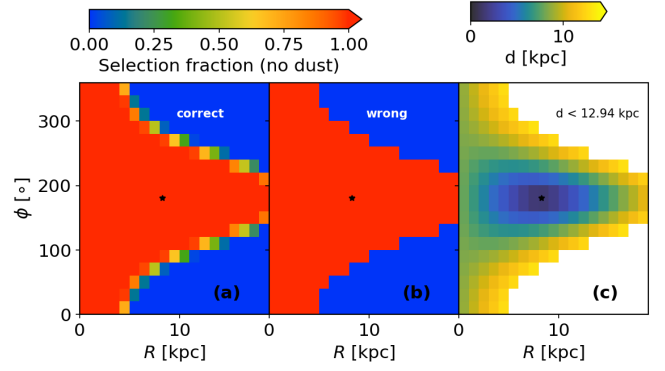


Fig. 13. Illustration of the selection function projected in ϕ - R space, for the case without dust at $Z_{GC}=0$ kpc (midplane). Panel (a) shows the map of the selection fraction computed using the sub-binning method, panel (b) shows the same for the method without sub-binning, while panel (c) shows the distance to all voxels that are within a distance of $d_{max} < 12.94$ kpc of the Sun. Panel (a) also shows the additional voxels that would be missed by assuming the median values of observables (l, b, G). In all panels, the location of the Sun is indicated by the black star.

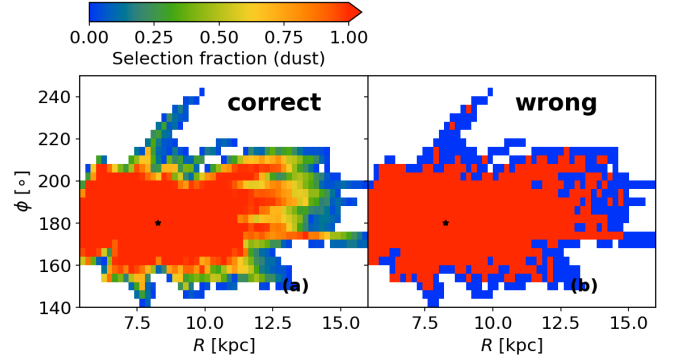


Fig. 14. Illustration of the effective volume projected in ϕ - R space, for the case with dust. Panel (a) shows the map of the selection fraction computed using the sub-binning method, showing a continuum of probability between 0 (unobservable) and 1 (fully observable). In panel (b), we show the same voxels as in panel (a), but for these the selection fraction is shown for the method without sub-binning. This shows that several voxels from panel (a) that have a probability of being observed would be considered unobservable or completely observed using the incorrect method of estimating the selection function. In both panels, the location of the Sun is indicated by the black *.

in Figure 13(b) (= 0 or 1), there is a set of voxels along the edge (where $d = d_{max}$) where some fraction of the voxel is still observable. Thus the sub-binning approach allows us to account for estimating the effective volume of a voxel and correctly include this region in our model.

This effect is drastic in the presence of dust, as is illustrated in Figure 14, where again we show the projection of voxels in ϕ vs. R . In panel (b) we show all the voxels that should be observable but colour-coded by the incorrect binary selection function that does not take into account the finite size of the voxels. All the voxels coloured red have a selection probability of 1, while those in blue have a selection probability of 0, in the incorrect approach, thus only the red voxels would have been predicted to be observable. In panel (a), the same voxels are presented but instead colour-coded using the correct method, now also taking into account the extinction to each sub-voxel when checking if

its distance is within d_{\max} . Now instead of having a binary 1 or 0, the voxels have a continuous selection fraction between 0 and 1. This approach would then correctly predict some of the blue voxels from panel (b) to be truly observable, while some of the red voxels are only partially observable. Figure 14 illustrates the non-intuitive pattern that the variation of Galactic dust imposes on the region observable in the Milky Way.

Henceforth for all our analysis, we use the sub-binning method described above to estimate the effective (fractional) volume of each voxel. For the observational data, we use the magnitude limit in the G band 17.5 from Figure 6, and the absolute magnitude is sampled from a *Gaussian*, that is, the luminosity function of the RC is taken as $LF_{RC} = \mathcal{N}(\bar{M}_G, \sigma_{\bar{M}_G})$, where $(\bar{M}_G, \sigma_{\bar{M}_G})$ is taken from Table 1. Thus compute the first layer of the selection function given as the fractional effective volume of each voxel as:

$$F_i = F_i(m_\lambda < m_{\lambda, \text{lim}} | LF_{RC}). \quad (19)$$

b.) *Gaia* selection function: Besides the probability that an RC like star can be observed given the magnitude limit of our sample, we also need to consider the probability that a source can be observed by *Gaia* at all. We term this the top-level selection function ($S_{\text{top},i}$). Cantat-Gaudin et al. (2023b) modelled the completeness of *Gaia* by comparing to the much deeper DE-CAPS survey (Schlafly et al. 2018). They were able to devise a single parameter called M_{10} that encapsulates the completeness based on only three observables, the sky position and magnitude (l, b, G). For our grid, we can compute the M_{10} for every voxel using the aforementioned sub-binning approach, and thus get the top-level selection function for every sub-voxel. We do this by using the *GaiaUnlimited Python* package⁵, and the class *DR3SelectionFunctionTCG*, using the central values of (l, b, G) in each sub-voxel. In any case, given our G magnitude limit of 17.5, $S_{\text{top},i}$ will be equal to 1, except in the most crowded fields.

Our parent dataset *gdr3wise* is a cross-match between the *Gaia* and *AllWISE* surveys. More specifically, every source in our parent catalogue is present in *Gaia*, and we are using the subset of stars that also have *AllWISE* photometry. In addition, we require that our stars have a measured parallax, so in summary we require all stars to have a finite ($l, b, \varpi, G, W1$). Essentially, all these filters are introducing selection effects of their own. To account for this we can compare the number of stars in the catalogue before and after applying the selection criteria, in bins of *Gaia* observables. This characterises the completeness as a function of quantities such as sky position and G magnitude. This ratio-ing method allows us to build a sub-selection function (since we can safely assume every source we study here is observed by our principal survey *Gaia*). Castro-Ginard et al. (2023) developed such a methodology to estimate the selection function for different subsamples of stars in the *Gaia* catalogue. This is done by comparing the number of stars in a given subsample to that in the overall *Gaia* catalogue, providing an estimate of the subsample membership probability ($S_{\text{sub},i}$) as a function of observables of choice. In the *GaiaUnlimited* code, the *SubsampleSelectionFunction* class uses a *beta-binomial* estimator to convert the number count ratios into a probability for a source to end up in the subsample. We choose to compute the ratios in bins of sky position and magnitude (l, b, G) only. In Appendix C we show the query that is run on the *Gaia* archive that allows us to compute this sub-selection function, and we show in Figure C.1, the sky projection of the completeness for a bright ($12 < G < 13$) and a faint $16 < G < 17$ magnitude bin, at *HEALPix* level 5. The

⁵ <https://gaiaunlimited.readthedocs.io/en/latest/>

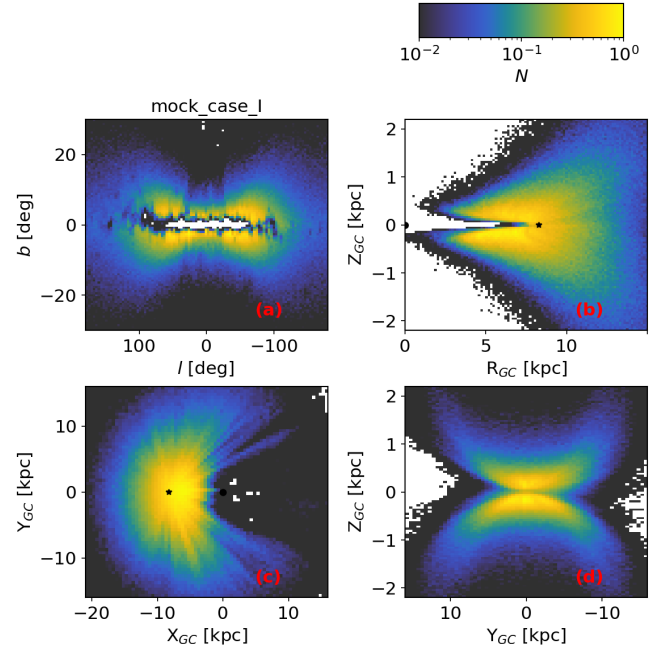


Fig. 15. Mock case I: Density distribution for the example with a single exponential disc that is also flared, for magnitude limit $G = 17.5$. A dust model is applied to the sample, as is evident in galactic coordinates (l, b) in panel(a) with the gap at very low latitudes. Panels (b,c,d) show the corresponding spatial distribution in cartesian Galactocentric coordinates. The locations of the Sun (star) and Galactic center (dot) are indicated by black points.

sub-selection function estimator relies on binning and computing number ratios, so naturally the more dimensions one would bin data in, the fewer stars there would be per bin, thus increasing the variance in the estimated selection function. We find that the selection function for the RC hardly varies with colour ($G - R_p$), and so ignoring this dimension allows us to have a more robust number statistic on the sub-selection function. The overall selection function is then a product of the individual layers,

$$S_i = F_i(m_\lambda < m_{\lambda, \text{lim}} | LF_{RC}) \times S_{\text{top}}(l, b, G) \times S_{\text{sub}}(l, b, G). \quad (20)$$

3.3. Generating mock data

For the purpose of validating our methodology, we generate mock data sets for which we know the true values. These are simplified models whose formulations are consistent with our model assumptions, and thus ideal test cases for validating our procedure.

For a given density model, the total number of stars can be computed by integrating over the volume of the survey,

$$N = \int N([R, z](l, b, \mu) | \Theta) \times \frac{d_{\text{hc}}^3 \log(10)}{5} \times S_i \, d\mu dl db \quad (21)$$

where $N([R, z](l, b, \mu) | \Theta)$ is the number density as before but for a given line-of-sight (l, b) and at distance modulus μ . To generate a mock catalogue, we sample $(l, \sin(b), \mu)$ from the density models, and thus need the Jacobian $|j(XYZ : lb\mu)| = \frac{d_{\text{hc}}^3 \log(10)}{5}$. The S_i is the effective selection function of the mock catalogue. Say, for example, if we generate a mock that is magnitude limited, has a sky dependent selection function, and is restricted only to the Red Clump, the net selection function would be,

$$S_i = F_i(m_\lambda < m_{\lambda, \text{lim}} | LF_{RC}) \quad (22)$$

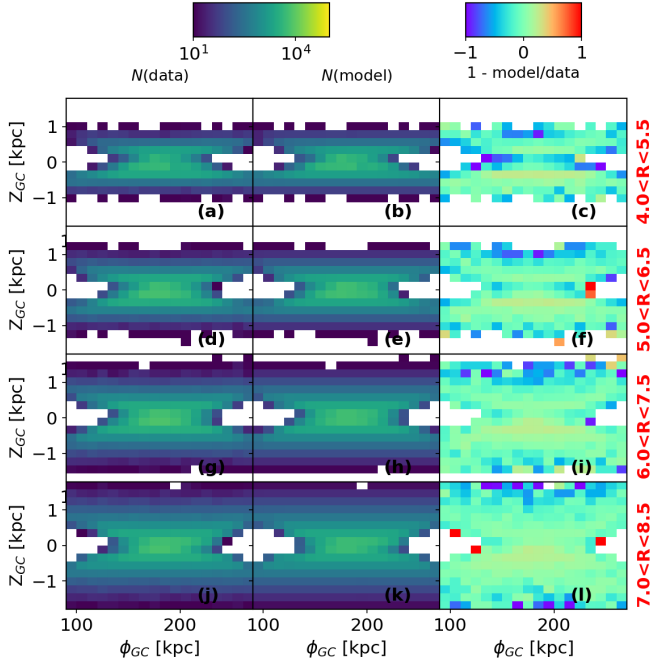


Fig. 16. Mock case I: Fitting residuals shown in the ϕ - Z_{GC} projection. Panel (a) shows the number density (logarithmic scale) of the mock data, panel (b) shows the predicted number density of the best-fitted model, and panel (c) shows the residual (relative to mock data). Panels (a-c) are restricted to $4 < R < 5.5$ kpc. The subsequent rows show the same information but for selected successive bins in R .

where LF_{RC} is the luminosity function (absolute magnitude distribution) of the Red Clump. In Figure 2, we showed the *CaMD* distribution of the RC from *Galaxia*. The marginalised distribution of absolute magnitude (right insets) shows that both M_G and M_{W1} can be approximated as quasi-Gaussian. Therefore, for the rest of the paper, we adopt a *Gaussian* LF_{RC} , $N(\bar{M}_\lambda, \sigma_{\bar{M}_\lambda})$, using values from Table 1. One could also simplify the method by adopting a *delta* function, $\delta(M_\lambda - \bar{M}_\lambda)$, in which case we would assume all RC to have a singular absolute magnitude.

We use the multidimensional sampler, *sampleNdim*, from the *AGAMA* code (Vasiliev 2019) to then generate our mock catalogue of 1 million sources. We convert from the heliocentric to the galactocentric frame, as described in subsection 2.2, but for the mock we here assume $Z_\odot = 0$ kpc. In subsection 4.1 we generate several versions of the mock catalogue, to demonstrate how our model fitting methodology performs for a range of Galactic parameters, magnitude limits, as well as with and without having applied extinction.

3.4. Fitting

We first grid all data in 3D space $(\Delta R, \Delta \phi, \Delta Z_{GC}) = (0.25 \text{ kpc}, 10^\circ, 0.25 \text{ kpc})$ kpc. Then, using the model described in subsection 3.1, we predict the counts in each bin $N_{i,raw}$. These "raw" counts predicted by the model need to be corrected, taking into account the selection function i.e., $N_i = N_{i,raw} \times S_i$. Then we compare the predicted and the observed counts per bin by maximising a *Poisson* log-likelihood (Bennett & Bovy 2019),

$$\ln p(N_{obs}|N) = \sum_i [-N_i + N_{obs,i} \ln(N_i)], \quad (23)$$

with the *emcee* package (Foreman-Mackey et al. 2013). We use $\max(25, 7 \times N_{dim})$ walkers and up to 5000 iterations. We perform the model fitting only over those voxels with $N_{obs,i} > N_{min,i}$,

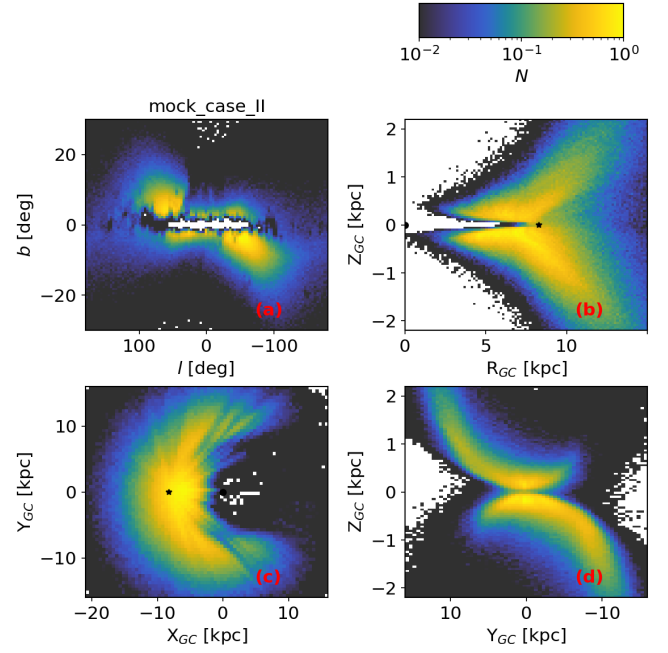


Fig. 17. Mock case II: Density distribution for the example with a single exponential disc that is also both flared and warped, for magnitude limit $G=17.5$. A dust model is applied to the sample, as is evident in galactic coordinates (l, b) in panel (a) with the gap at very low latitudes. Panels (b,c,d) show the corresponding spatial distribution in Cartesian Galactocentric coordinates. The locations of the Sun (star) and Galactic center (dot) are indicated by black points.

i.e., with counts above a minimum threshold. For the mock data we generate 1 million particles in all, and use $N_{min,i}=10$, while the observational dataset is of the order of 10 million stars, and there we choose $N_{min,i}=100$ as the nominal value, but vary it to estimate the uncertainties in our parameters (see subsubsection 4.2.2). In order to visualise our best-fit, we inspect two dimensional projections of the number counts. Specifically, we compare the surface density Σ_{surf} vs. R , for the data and the model, in bins of $\Delta R = 0.25$ kpc, to inspect the radial profile of number counts. Similarly, we compare $N(z|R)$ vs. Z_{GC} , for the data and the model, in bins of $\Delta Z_{GC} = 0.25$ kpc, at different R , to inspect the vertical profile. Finally, we consider the projection in ϕ - Z_{GC} at various R , moving from the inner to the outer disc. This is to inspect if our model is able to fit azimuthally varying features in the data.

4. Results: Density Modelling

4.1. Fitting Mock data

We begin by demonstrating our model fitting method on a mock catalogue of RC stars, that were generated as described in subsection 3.3. We tested our method on several different test cases, but for demonstration we here restrict ourselves to two cases discussed below. In both cases, we only consider the selection function layer due to extinction and the top level *Gaia* selection function, since the sub-sample selection does not apply to our simple mock density model.

Case I: We generate a mock galaxy of 1 million particles with a 1 disc component and no warp. The density profile is described by an exponential in both R and Z_{GC} . Additionally, this galaxy has a flare, and we impose a magnitude limit of $G=17.5$.

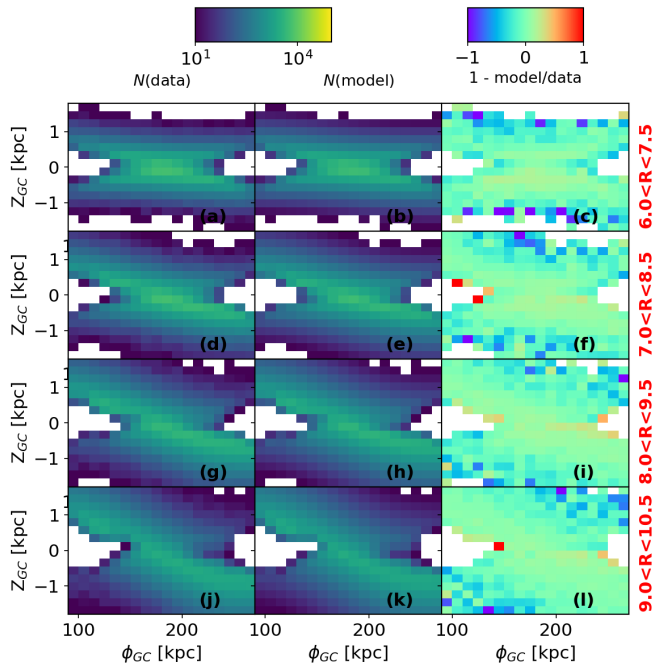


Fig. 18. Mock case II: Fitting residuals shown in ϕ - Z_{GC} projection. Panel (a) shows number density (logarithmic scale) of the mock data, panel (b) shows the predicted number density of the best-fitted model, and panel (c) shows the residual (relative to mock data). Panels (a-c) are restricted to $6 < R < 7.5$ kpc. The subsequent rows show the same information but for selected successive bins in R .

In order to exaggerate the effects of extinction we choose to use here the 2D dust model of S98 instead of the 3D model described in subsection 2.3. Finally, we convolve the simulated distance modulus (μ), with typical RC distance uncertainties (see subsection 2.4). The true parameters for this disc are $(R_d, h_{z,\odot}, \log_{10} R_{fl}[\text{kpc}]) = (3.3 \text{ kpc}, 0.3 \text{ kpc}, 0.6)$. The density maps of the mock are shown in Figure 15, with the projection in Galactic coordinates (l, b) in panel (a), in R - Z_{GC} (to show the flare) in panel (b), and in Cartesian Galactocentric coordinates (X_{GC}, Y_{GC}, Z_{GC}) in panels (c) and (d). In Figure D.1 we show the corner plot from the MCMC fitting carried out for this example disc, where we had set $N_{\min,i} = 10$. The best fit values are indicated with vertical lines, and agree very well with the input values for the mock. To better judge the fit, we also show the projection in ϕ - Z_{GC} space in Figure 16 of the mock data and the fitted model for Galactocentric radial bins between $4 < R < 8.5$ kpc (columns 1 & 2). Also shown in Figure 16 are the residuals between the mock data and model (column 3). The colour map of the residuals shows general good agreement except at the edges of the density distribution where the number of stars drops rapidly.

Case II: The second example we include is that of a disc which is warped, described by $(\phi_w, R_w, a_w, h_{w0}) = (170^\circ, 6.5 \text{ kpc}, 1.0, 0.3 \text{ kpc})$. This is a rather extreme warp ideally oriented for the purpose of illustration and testing, and is not meant to represent the warp of the Milky Way. The rest of the parameters are identical to the disc in case I. Figure 17 shows the density maps for this mock data, where a tilt (top left to bottom right) is apparent in the (l, b) map in panel (a). This can be compared to Figure 15(a) where the disc was not warped. In cartesian coordinates, the sense of the warp here is such that the disc bends up (towards positive Z_{GC}) at positive Y_{GC} , and bends down at negative Y_{GC} , as shown in Figure 17, as expected for the line-of-nodes being at $\phi = 170^\circ$. Figure D.2 shows the corner plot

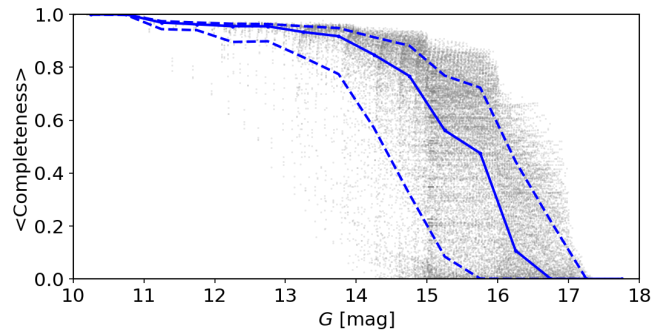


Fig. 19. Completeness for the RC sample for $R > 3$ kpc, shown in gray, as a function of G magnitude (0.5 mag bins), with the blue solid line showing the median profile and the dotted lines showing the 84th and 16th percentiles.

of the fit, again with the best-fit values indicated as blue lines. The mcmc procedure converges to recover the input values, although we do notice that the warp parameters (R_w , h_{w0} and a_w) show strong correlations between them. The ϕ - Z_{GC} projection of this dataset is also shown in Figure 18, again for three successive bins in R , though here we note that the density map shows a diagonal feature beyond $R > 7$ kpc that is the imprint of the warp. The residual maps are again mostly close to zero across the pixels, except at the very edges (low number statistics), and thus show that the fitting works well in this case too, and we are able to fit both for the structural (scale-length/height) and shape parameters (warp) of the disc, though these later show significant correlations.

4.2. Observational data

4.2.1. Selection function & Completeness map

We now move on to fitting our model on the *gdr3wise*[RC] dataset. Following subsection 3.2, we apply all three layers of the selection function to the real data. The predicted completeness of the RC sample as a function of G magnitude is shown in Figure 19, with the solid blue line indicating the median profile and dotted lines showing the variance in completeness. As this profile (blue line) is averaged over the entire volume (grid), we expect to see variance at any given radius. Overall, the RC sample is largely complete (close to 1) down to about $G = 14$, falls to about 0.5 completeness at $G = 16$, and then drops sharply to 0 by $G = 17$.

As mentioned in subsection 3.2, taking advantage that RC stars are standard candles, we can determine the fraction of RC stars in our sample (completeness) for any particular volume. In Figure 20, we show the completeness in polar coordinates (R, ϕ) , averaged over three different slices in Z_{GC} . Towards the inner Galaxy, the completeness drops sharply due to extinction, while in the anticentre direction the completeness extends much further. While overall the two maps at $Z_{GC} > 0.25$ kpc and $Z_{GC} < -0.25$ kpc exhibit very similar completeness, there are minor differences between the two due to the asymmetrical dust distribution above and below the disc. Figure 20(b) shows the completeness for the midplane region, $|Z_{GC}| < 0.25$ kpc. Compared to the maps at higher Z_{GC} , the region of high completeness covers a much smaller region. Indeed, in the plane we are most affected by dust, obscuring our view toward the inner Galaxy, and along other lines-of-sight with high extinction. In addition, we are also affected by high source crowding toward the Galactic

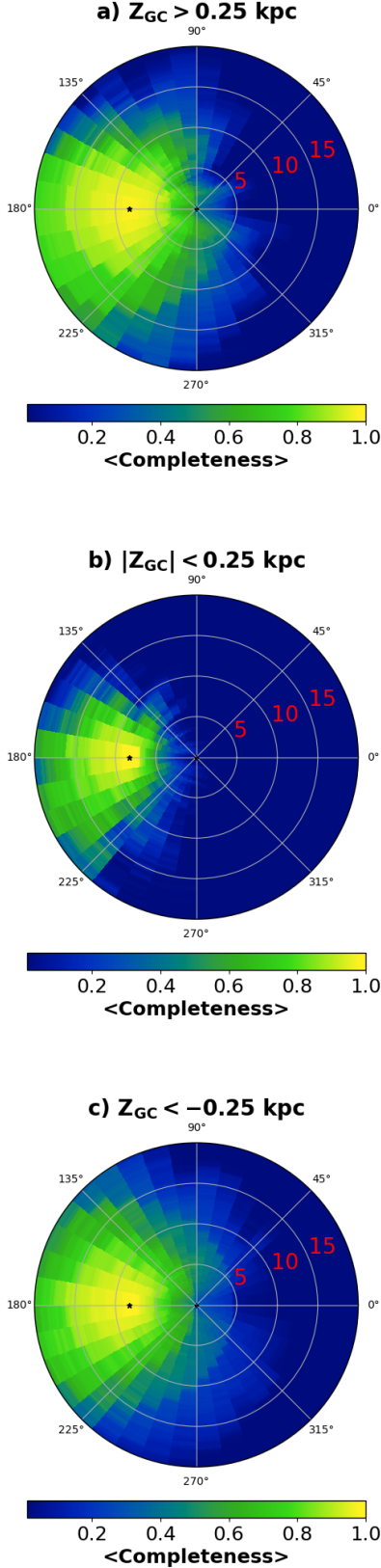


Fig. 20. The completeness for RC stars over the entire grid shown in galactocentric polar coordinates (ϕ, R), for three slices in Z_{GC} , above the plane (panel a), in the midplane (panel b), and below the plane (panel c). The concentric circles indicate bins in R , with values in kpc denoted in red, and the black star indicating the Sun's position.

Table 4. Best fit values for the parameters fitted to observational data. Model 1 only fits for a single exponential disc that is also flared. Model 2 fits for two exponential disc components, with only one allowed to be flared.

| Model 1 parameter | Best-fit value |
|--------------------------------|---------------------|
| R_d | 3.26 ± 0.25 kpc |
| $h_{z,\odot}$ | 0.40 ± 0.03 kpc |
| $\log_{10} R_{fl}[\text{kpc}]$ | 1.63 ± 0.20 |
| Model 2 parameter | Best-fit value |
| R_d | 3.56 ± 0.32 kpc |
| $h_{z,\odot}$ | 0.17 ± 0.01 kpc |
| $\log_{10} R_{fl}[\text{kpc}]$ | 0.37 ± 0.04 |
| R_{d2} | 2.59 ± 0.11 kpc |
| $h_{z2,\odot}$ | 0.45 ± 0.11 kpc |
| f_{d1} | 0.36 ± 0.02 |

center, which makes it difficult for *AllWISE* to resolve individual sources, and thus making these fields less well sampled. Nevertheless, all three maps show that we are able to map out a large portion of the disc out to at least $R = 15$ kpc with fairly high completeness. An interactive three-dimensional visualisation of completeness for our RC sample is provided on the *GaiaUnlimited* webpage⁶.

4.2.2. Fitting model to data

Following the method used for the mock catalogues, we fit for the parameters listed in Table 3. In the first instance, we ignore the warp and check if we can fit the distribution with only a single flaring disc (i.e., we set $f_{d1} = 1$). The corner plot for this fit is shown in Figure E.1, where we find, $R_d = 3.26 \pm 0.20$ kpc, $h_z = 0.40 \pm 0.02$ kpc, and $\log_{10} R_{fl} = 1.60 \pm 0.20$. These are typical scale parameters for the old thin disc population Milky Way (e.g. Bland-Hawthorn & Gerhard 2016), but in this case we obtain a slightly higher h_z which compensates for a very weak flare. While the fit does converge, a closer look at the residuals shows that a single disc is not enough to account for the stellar density both in the inner ($3 < R < 10$ kpc), and the outer disc ($10 < R < 15$ kpc) simultaneously (see Figure E.2). We therefore allow for an additional disc component and fit for all the parameters (barring the warp again) listed in Table 3. The corner plot in Figure F.1, shows that the fit converges. Essentially, we find that the RC sample is best described by a two disc component model, with one component having $R_d = 3.56 \pm 0.32$ kpc, $h_z = 0.17 \pm 0.01$ kpc, and $\log_{10} R_{fl} = 0.37 \pm 0.04$. This is essentially a long and thin disc exhibiting a strong flare, and constitutes about 36% of the total mass. The second component is dominant ($\sim 64\%$) has a scale length of $R_{d2} = 2.59 \pm 0.11$ kpc and constant (non-flaring) scale height of $h_{z2} = 0.45 \pm 0.11$ kpc. When we included a flare parameter for this second disc, the fit was unable to constrain this, but this did not affect the values obtained for the remaining parameters, so we can assume that the thinner component is contributing alone to the overall flare in our dataset.

In order to estimate the uncertainties of our estimated parameters, we adopted a Monte-Carlo approach and ran the fitting over 10 realisations of the data, each time sampling the distance modulus from the assumed uncertainty distribution, $\mathcal{N}(\bar{\mu}_\lambda, \sigma_{\mu(W1)})$ as described in subsection 2.4. Then we used the 16th and 84th percentiles in each parameter to estimate the spread

⁶ Interactive 3D visualization of the RC completeness.

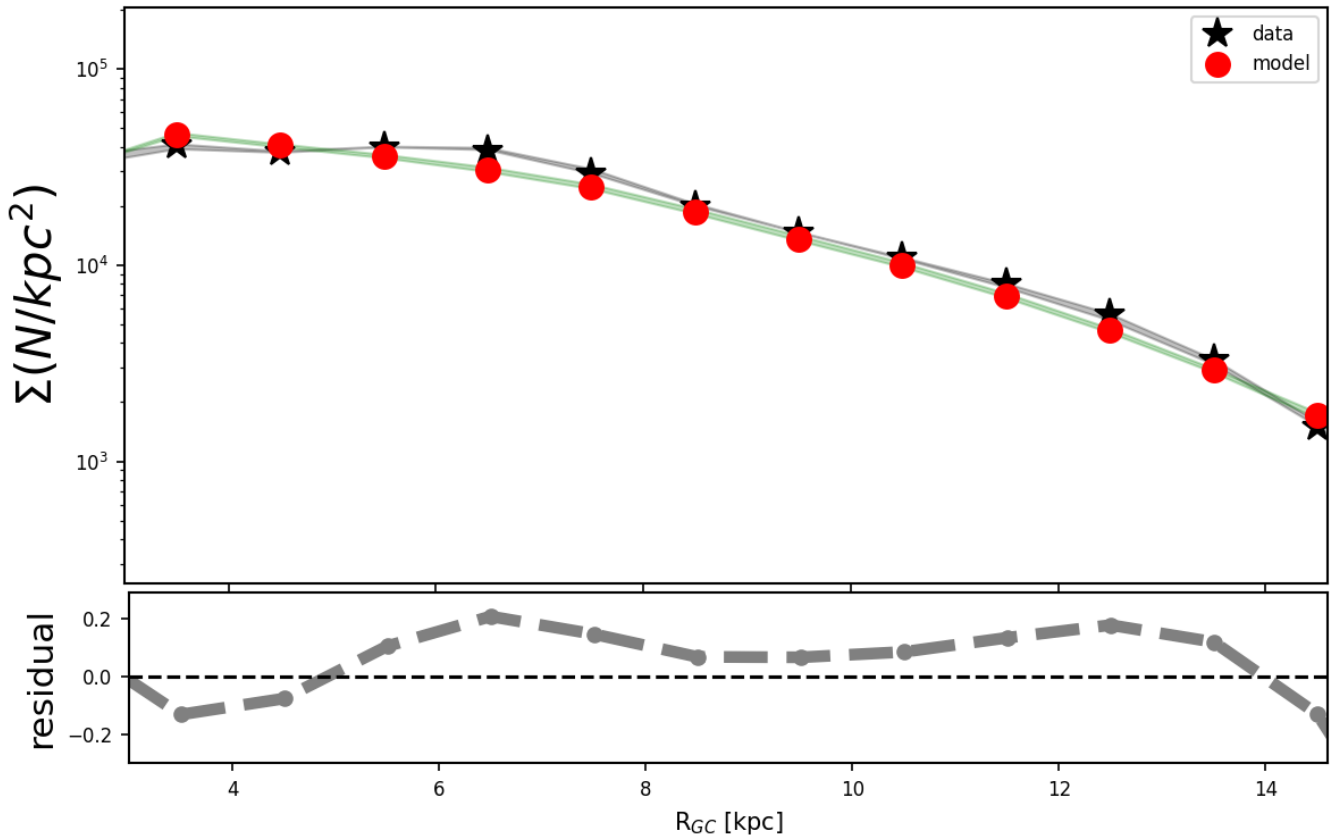


Fig. 21. Surface density of *gdr3wise*[RC] averaged over $|Z_{GC}| < 1$ kpc. Data is shown as black points, and the grey shaded area represents the 2 standard deviations over which each realisation of the data varies. The model predictions are shown in red and again the green shaded region represents the uncertainty in each bin. The residuals ($1 - \text{model}/\text{data}$) are shown in the lower panel.

in their median values. However, we found these uncertainties to be very small and therefore unrealistic. This is likely a consequence of using a very large sample of stars. Instead, just to estimate the uncertainty, we generate one realisation of the data, and then varied the arbitrarily chosen parameter $N_{\min,i}$ from 100 to 20 i.e., performed independent fits while varying the arbitrarily chosen minimum number of stars per voxel criterion. In general, the median values of the parameters remains very consistent for the different $N_{\min,i}$ values, but we note that scale-length of disc 1 drops from $R_d = 3.56$ kpc (at our nominal value of $N_{\min,i} = 100$) to $R_d = 3.24$ kpc ($N_{\min,i} = 20$). We use the variation in the parameter values between these two fits as uncertainty estimates. The best fit parameters and their uncertainties, for both models are summarised in Table 4.

Using these best fitting parameters, we take a closer look at the residuals between data and model, by considering projections in 1d and 2d spaces. First, in Figure 21 (upper panel), we show the surface density $\Sigma(N/\text{kpc}^2)$ as a function of R , with the model in red, which overall, is able to capture the profile of the data (stars). The grey lines in the background indicate the variation in surface density (observed and model) for each bin for every realisation of the dataset. There is a slight bump in the data around $R = 6$ kpc, and another one around $R = 12.5$ kpc, which are clearly not fit by the model, seen more clearly in the residuals (lower panel). Next, we consider the vertical counts, $N(Z_{GC}|R)$ as a function of $|Z_{GC}|$ in Figure 22, where we plot the number of stars in data (points) in 2 kpc wide annuli between $4 < R < 15$ kpc, and the model prediction as broken lines. Again, the model is largely able to capture the trends seen in the data profiles. We remind the reader that our fit was not performed in

these projected spaces, so we do not expect one-to-one agreement for every bin, but judge the fit on its ability to capture the overall trends. As noted before, the slope of $N(z_{GC}|R)$ flattens for $R \geq 12$ kpc, due to the flare in the disc.

Finally, we inspect the residuals in the ϕ - Z_{GC} projection for bins in R . We separately consider the inner disc ($3 < R < 10$ kpc), and the outer disc ($10 < R < 14.5$ kpc) in Figures 23 and 24 respectively. Figure 23 shows the ϕ - Z_{GC} projection for the inner disc, where each row corresponds to a radial bin, the first two columns show the number density of the data and model respectively, the third column shows the relative residual [$1 - (\text{model}/\text{data})$]. Considering the last column, we can see that overall our model is able to describe the data well, as most of the region in these panels is fairly uniform, with the exception of the edges of our grid due to low number counts and unaccounted for distance uncertainties, as mentioned before. There are other regions of high residuals however. In the inner-most annulus of Figure 23 we see the model is under-predicting the counts. This is likely because we don't include a separate component for the Galactic bar/bulge, which may be contaminating this bin. While the remaining panels show smaller residuals, we note in the panels in the range corresponding to $6.0 < R < 7.5$ kpc the model under-predicts the counts close to the Galactic plane. This feature gets weaker beyond 7.5 kpc. This shows that the excess of stars at this radius, noted above in Figure 21, is restricted close to the plane. As we move outwards in the $9 < R < 10.5$ kpc annulus, there is a weak presence of residuals along the diagonal, that is the data predicts larger counts w.r.t the model at positive Z_{GC} and $\phi < 180^\circ$, then at negative Z_{GC} and $\phi > 180^\circ$. This becomes more pronounced as we move to larger radii, as seen in

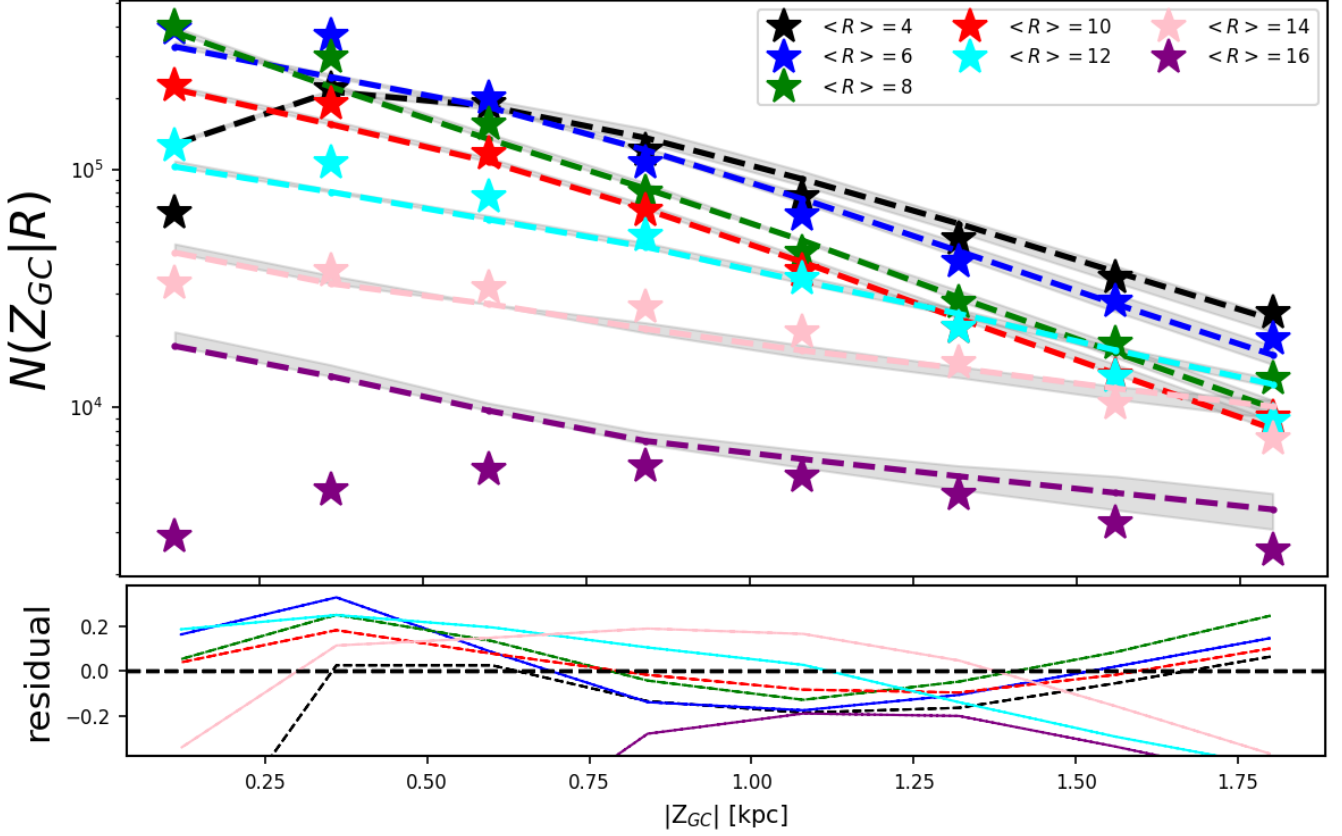


Fig. 22. Vertical counts as a function of $|Z_{GC}|$ at progressive annuli in R (2 kpc wide). In each case, the data is shown as stars, and the predictions from model 2 as dashed lines in the same colour. The uncertainties in the best-fit model are represented by the shaded grey area. The residuals between data and model are shown in the lower panel.

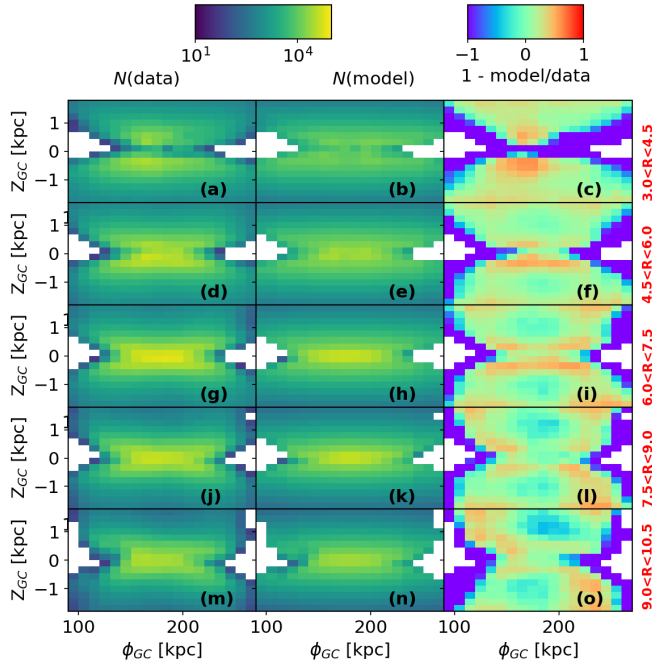


Fig. 23. Residuals between model 2 from Table 4 and data in the ϕ, Z_{GC} projection, shown for the inner disc region ($3 \text{ kpc} < R < 10.5 \text{ kpc}$). In each row, the first column shows the number density of the data, the second row shows the number density predicted by the model, and the third row shows the residuals relative to the data. Each row represents a 1 kpc wide annulus in R .

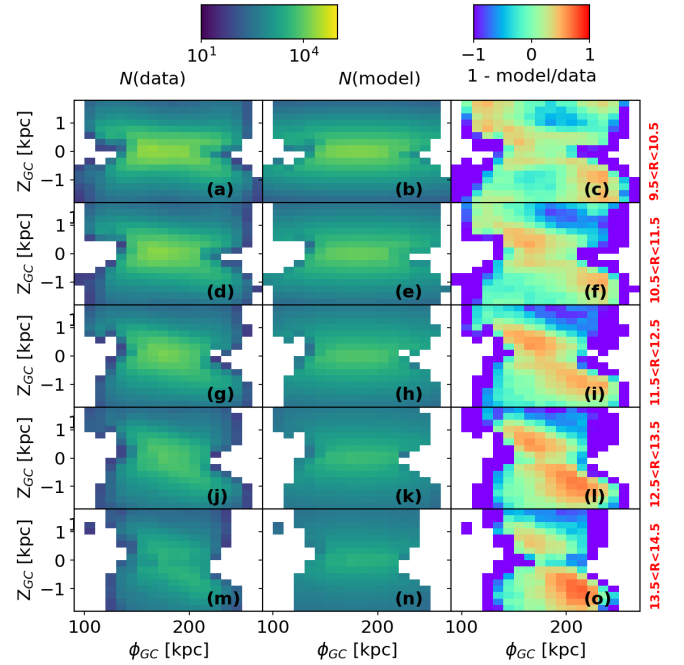


Fig. 24. Residuals between the model and data in the ϕ, Z_{GC} projection, same as Figure 23 but for the outer disc ($9.5 \text{ kpc} < R < 14.5 \text{ kpc}$).

Figure 24, where we see the model is severely under-predicting the counts along this diagonal with increasing R , particularly be-

yond $R > 10.5$ kpc. These residuals are clear evidence that the distribution of RC stars is warped in the outer disc.

In Figure 25, we show the relative residuals in polar coordinates (R, ϕ), averaged over three different slices in Z_{GC} . On these maps, white regions indicate where the data and the model are in close agreement, while red (model underpredicts) and blue (model overpredicts) highlight the discrepancy. We can identify three regions with discrepancy from the model prediction where the model is underpredicting counts. First, there is a small patch around $R < 3$ kpc along $\phi = 180^\circ$ seen in the slices above and below the Galactic mid-plane. This is likely to be due to the contribution from the bulge that we do not model for. The next feature is in the outer disc beyond $R > 9$ kpc. We note that this outer feature appears to shift to higher azimuth when comparing the residuals in the upper slice ($Z_{GC} > 0.25$ kpc) with respect to the lower slice ($Z_{GC} < 0.25$ kpc), shifting from $160^\circ < \phi < 180^\circ$ to $170^\circ < \phi < 210^\circ$. This is consistent with the residuals in the outer disc shown in Figure 24, where the residuals are seen to lie along a diagonal, that is, at positive Z_{GC} the residuals are higher than the corresponding negative Z_{GC} slice below the plane for $\phi < 180^\circ$. And again the residuals are higher below the plane for $\phi > 180^\circ$, compared to the corresponding Z_{GC} slice above, which we interpret to be the signature of the Galactic warp. However, we also see these residuals also shift toward higher radii with increasing azimuth, consistent with an overdensity with a spiral geometry similar to the outer arm of the 2-arm spiral model (solid black curves) of Drimmel (2000, hereafter D00) based on near-infrared (NIR) data.

For the inner disk ($R < 9$ kpc) the residuals show a clear and distinctive pattern only near the Galactic midplane ($|Z_{GC}| < 0.25$ kpc, Figure 25(b)). Here we see that the data has an under-density (shown in blue) with respect to the axisymmetric model, seen approximately at the Sun's position and following the dotted curve that indicates the inter-arm position where the density is expected to be a minimum between the two arms. Inside this curve we again see positive residuals, though it is less clear whether these residuals follow a spiral geometry that is expected from the NIR-based model. Indeed, the inner edge of the positive residuals, approximately delimited by the inner spiral arm, is probably largely determined by extinction severely limiting how far we can reliably map the RC sample. In any case, any hint of spiral geometry in the inner-disc residuals is not clearly evident above ($Z_{GC} > 0.25$ kpc) and below ($Z_{GC} < -0.25$ kpc) the Galactic plane (upper and lower panels of Figure 25).

4.2.3. Testing warp parameters with real data

As discussed in the previous paragraphs, the best-fit of our assumed axisymmetric model exhibits diagonal residuals in the ϕ - Z_{GC} projection. It is natural to wonder then whether the warp of the Milky Way can account for this outer feature.

To check this we tried to simultaneously fit for a model which included all the parameters from Model 2 (Table 4) as well as the additional four warp parameters (ϕ_w, a_w, R_w, h_{w0}). However, the MCMC routine did not converge for these warp parameters, but interestingly, the remaining best-fit parameters did not significantly differ from Model 2. We then locked the best-fit parameters from Model 2, and only ran a fit for the four warp parameters, but again the MCMC had trouble converging. Our tests showed that the fit was in particular unable to constrain two parameters, a_w , and ϕ_w which indicates the line-of-nodes (LON) for the warp. However, recent works have shown that the Milky Way's warp does not have a constant LON, and that it curves towards lower ϕ beyond about $R = 12.5$ kpc (Dehnen et al. 2023;

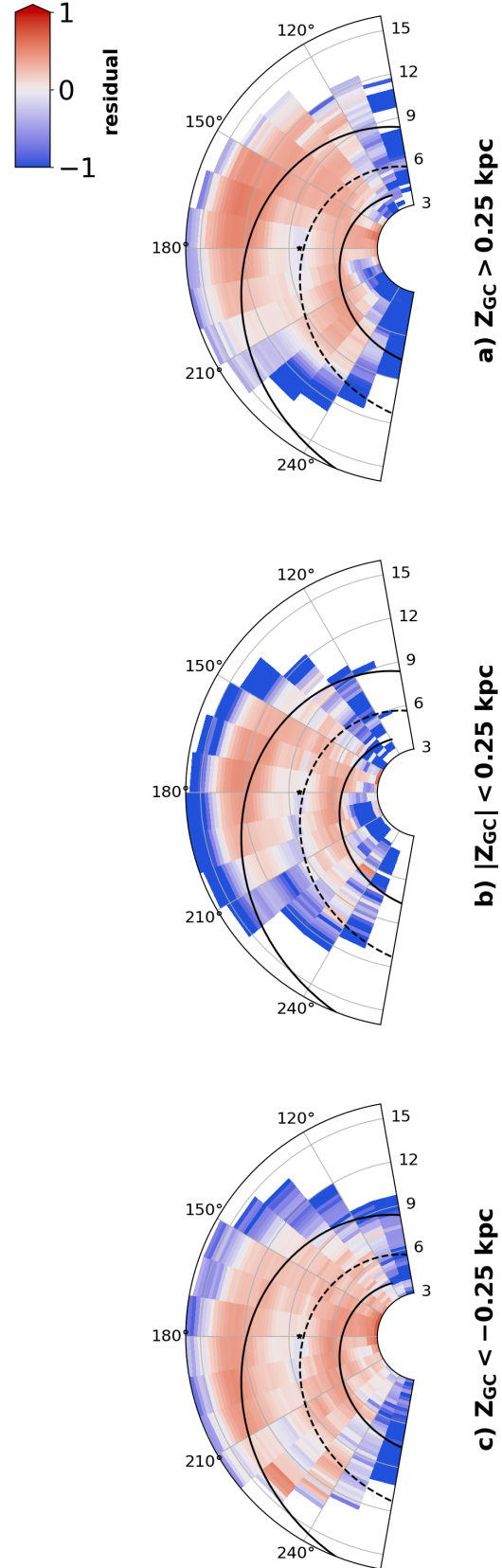


Fig. 25. Relative residual ($1 - \text{model}/\text{data}$) for Model 2 from Table 4, applied to *gdr3wise*[RC], and shown in polar coordinates. The residuals are shown for three slices in Z_{GC} , above the plane (panel a), in the mid-plane (panel b), and below the plane (panel c). The 2-arm NIR spiral model from Drimmel (2000) is overplotted as black curves.

Cabrera-Gadea et al. 2024; Jónsson & McMillan 2024; Poggio et al. 2024). This could possibly explain in part why we are unable to constrain the ϕ_w as our warp parametrisation assumes a single LON for simplicity.

Figure 24 shows that the diagonal feature already starts appearing around $R=9.5$ kpc, i.e., well inside the regime where a constant LON is reasonable to assume. So, instead of adjusting all warp parameters simultaneously, we fit for only two (R_w , h_{w0}), while keeping the other two fixed within the range of values found in the literature, at $\phi_w = (178^\circ, 170^\circ)$, and $a_w = (1.0, 2.0)$. Figure 26 shows the corner plots for four of these configurations, where we find $R_w=8.6$ kpc for $(\phi_w, a_w) = (170^\circ, 2.0)$, and $R_w=9.8$ kpc for $(\phi_w, a_w) = (178^\circ, 1.5)$. Essentially, assuming that the LON of the warp varies between 2 to 10 degrees from the Galactic anti-centre allows us to place constraints on the onset of the warp at between $8.6 < R_w < 9.8$ kpc. In Figure 27 we show the relative residuals in ϕ - Z_{GC} projection in the outer disc for these four configurations. Each column corresponds to one configuration, covering the $9.5 < R < 14.5$ kpc part of the disc. Figure 27 shows that, after having allowed for a warp, the residuals along the diagonal are much weaker.

Figure 28 shows different estimates of the warp amplitude available in the literature, together with the amplitude obtained with our sample, shown as a black shaded area for different assumed values of ϕ_w (between 170° and 178°) and a_w (between 1 and 2). As we can see, for $R \gtrsim 12$ kpc (grey shaded area) the difference between the obtained warp amplitudes for different assumed a_w and ϕ_w is quite large, reaching a variation of more than 1 kpc at $R \sim 14$ kpc. This indicates that we are not able to reliably constrain the amplitude of the warp beyond that radius.

For $R \lesssim 12$ kpc, we note that our obtained warp amplitude is in broad agreement with the parametrizations by Uppal et al. (2024), based on RC stars, and Cheng et al. (2020), based on general stellar populations in Gaia DR2 / APOGEE, but larger than the estimate from López-Corredoira et al. (2002), again based on a selection of Red Clump stars. This latter estimate is in better agreement with the amplitude seen in the young giants (Poggio et al. 2024) and Cepheids (Chen et al. 2019) (See also other warp parametrizations based on Cepheids, e.g. Skowron et al. 2019; Dehnen et al. 2023; Cabrera-Gadea et al. 2024, whose estimated warp amplitudes are consistent with the Cepheid's warp amplitude shown in Figure 28.)

5. Discussion

Our best-fit model suggests that the RC stars are found in a two component disc (Table 4, Model 2), with a long ($R_d \sim 3.56$ kpc) and thin disc that is also flared and potentially warped. This disc describes the stellar distribution from the Solar circle and beyond, while a second thicker and shorter ($R_d \sim 2.59$ kpc) component that constitutes about 64% to the disc mass, describes well the distribution from $3 < R < 8$ kpc. There have been several studies mapping the scale parameters of the disc, and using a wide variety of tracers. Using flux maps in the near Infrared from the COBE satellite, Drimmel & Spergel (2001) found a scale-length of about 2.31 kpc, which is close to that we find for the dominant component, possibly tracing the old thin disc. Recent studies include that by Binney & Vasiliev (2024, BV24), who combined *Gaia* DR3 with chemistry from *APOGEE*-DR17, and distances from the *StarHorse* catalogue (Queiroz et al. 2023), to produce a chemodynamical model of the Galaxy using action-based distributions $f(\mathbf{J})$. In their analysis they treat the Galaxy as a composite of several disc components, and in their Table 3 list the best-fit parameters for components of the Galactic disc, split

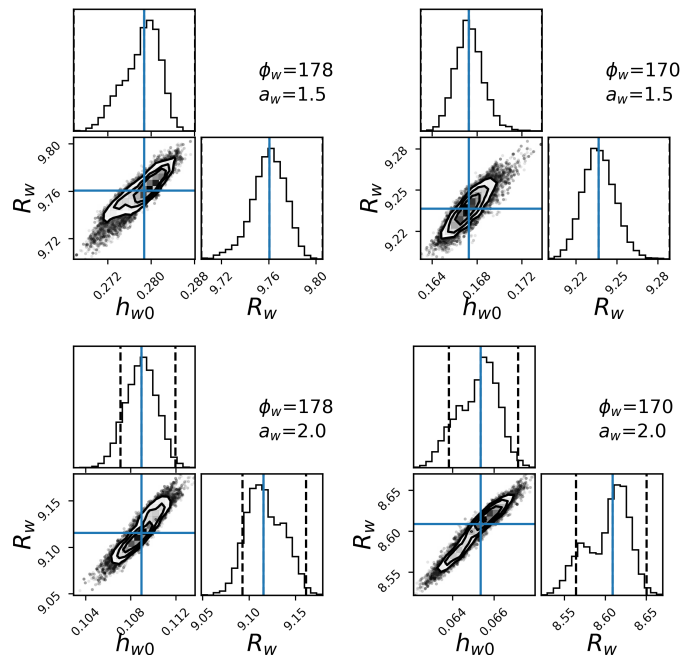


Fig. 26. Posterior probability distributions for two warp parameters (R_w, h_{w0}), assuming Model 2 (Table 4), applied to *gdr3wise*[RC]. We show four cases where the other two warp parameters (ϕ_w, a_w) have been fixed.

by age. They provide $J_\phi / v_{\text{circ}}(R_0) = R_d$, where J_ϕ is the angular-momentum of stars. They find that the old disc has a scale-length of about $R_d = 2.12$ kpc, while the younger discs are at about $R_d = 4$ kpc. Essentially, scale-length was found to decrease with age. Without an age dissection, they find $R_d = 3.6$ kpc, but this also includes the much older bulge component. Our parameters are broadly in agreement with their analysis. Using the APO-K2 asteroseismic catalogue, Warfield et al. (2024) recently derived the age of RGB stars, and showed that the RC in the traditional thin disc (α -poor) has a broad age distribution with a peak around 3-5 Gyr, while the age distribution of the RC in the traditional thick disc (α -rich) seems to be much flatter. This blurs the distinction between the old and young disc because, as they point out, the Galaxy seems to have many young α -rich RC stars that may have gained α -rich material through mass accretion in close binaries (Grisoni et al. 2024; Yu et al. 2024). Using high fidelity spectroscopic parameters from *APOGEE*, Lian et al. (2024) studied the surface density profiles of mono-abundance populations in the disc in bins of ages. They find that in the inner disc $3.5 < R < 7.5$ kpc, the surface density profile is very flat, in agreement with high redshift Milky-Way type galaxies, while the region outside is best described by a single exponential with $R_d = 2.6$ kpc. For our sample, the measured surface density profile shown in Figure 21 also shows a flatter profile inside of $R < 7$ kpc, however, this is in the observed data-space and so does not necessarily correspond to a flatter profile in the underlying model.

The vertical counts in the RC disc are generally well traced by the parameters of our Model 2, as shown in Figure 22. In the observed counts (starred points), there is a hint of a flare i.e., change in slope of $N(z|R)$ as a function of $|Z_{GC}|$. Specifically, we find $\log_{10} R_d[\text{kpc}] \sim 0.37$ for the disc we allow to be flared in Model 2. Figure 29 shows the predicted profile of the scale-height as a function of R for disc1 in our model, shown as black curves for both the single disc (dotted curve) and double disc model (solid curve). Also plotted here (as dashed curves)

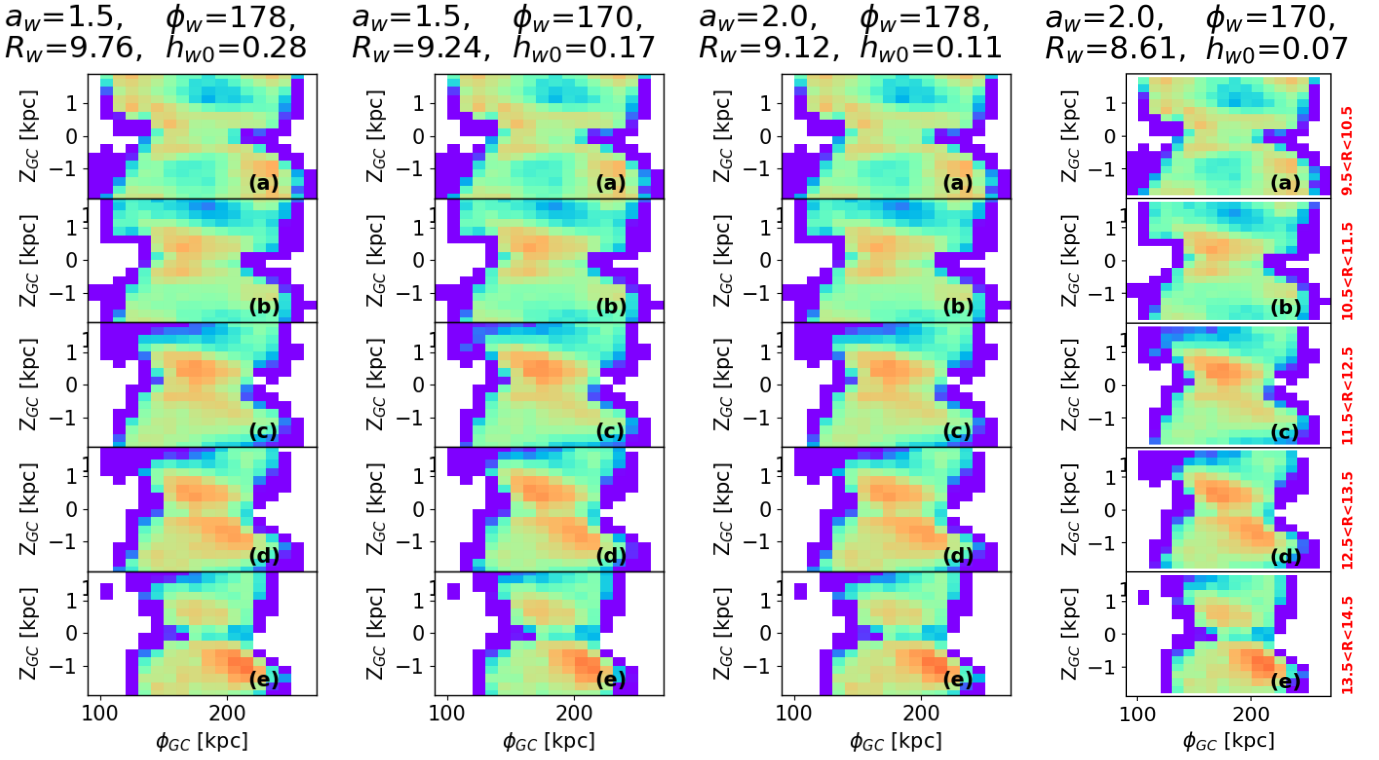


Fig. 27. Relative residual (1-model/data) for *gdr3wise*[RC], corresponding to the four cases exploring warp parameters shown in Figure 26. For each case, we show the residuals in successive R annuli ($9.5 \text{ kpc} < R < 14.5 \text{ kpc}$).

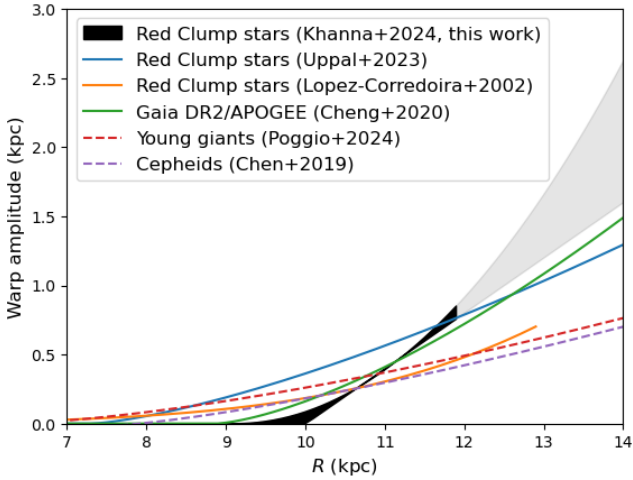


Fig. 28. Comparison between the warp amplitude obtained in this work and other parametrisations available in literature, based on different stellar tracers. The black shaded area shows the warp amplitude obtained in this work, in the region where our dataset and our adopted approach allow us to reasonably constrain the warp shape. At larger Galactocentric radii ($R \gtrsim 12 \text{ kpc}$, grey shaded area), it is not possible for our approach to give a reliable estimate of the warp amplitude based on our dataset, due to the lack of convergence of the fitting routine (see discussion in the text).

are a few profiles of the scale-height from the literature for tracers including and other than the RC. López-Corredoira et al. (2002, LC02 hereafter) studied the disc in the NIR using data from *2MASS* where the sample is dominated by RC like stars. They found the normalisation $h_{z,\odot} = 0.31 \text{ kpc}$, and a flare parameter of $\log_{10} R_{\text{fl}} = 0.53$ (blue curve). More recently, combin-

ing both *2MASS* and *Gaia*, Uppal et al. (2024, U24 hereafter) also constructed an all-sky RC sample and found $h_{z,\odot} = 0.35 \text{ kpc}$, but a weaker flare parameter of $\log_{10} R_{\text{fl}} = 0.85$ (red curve). Cantat-Gaudin et al. (2024, TCG24 hereafter) fit for density profiles of a combined *Gaia*-*APOGEE* sample of RC stars for which high quality spectroscopic parameters are available. This allowed them to study the profiles by population, specifically by metallicity. Crucially, their model fitting takes into account the complex selection function of the combined sample. In the range $-0.3 < [\text{Fe}/\text{H}] < 0.4$ where we expect most of our RC stars to be populated, they find $0.24 < h_{z,\odot} < 0.31 \text{ kpc}$ with the flare ranging between $0.64 < \log_{10} R_{\text{fl}} < 1.09$. In Figure 29 we include the results from TCG24 as a shaded grey region, showing the span of the flare parameter between -0.3 (lower bound) $< [\text{Fe}/\text{H}] < 0.3$ (upper bound). Except for U24, all studies also use an exponential parameterisation for the flare similar to us. However, all the aforementioned studies only consider a single disc component in their fitting procedure. Our value of $\log_{10} R_{\text{fl}} = 0.37$ is smaller than the aforementioned studies, which would indicate a stronger flare than previously found, though looking at Figure 29, the profile is not too dissimilar to that found by LC22, except we have a smaller normalisation of $h_{z,\odot} = 0.17 \text{ kpc}$.

In their best fitting model, BV24 also provide the scale-heights of the numerous disc components in terms of their vertical action as $h_{z,\odot} = 0.012 \times J_{z,0}$ (Binney & Vasiliev 2023). They find that their old disc has $h_{z,\odot} \sim 0.28 \text{ kpc}$, while the high- α component has $h_{z,\odot} = 0.78 \text{ kpc}$. Interestingly, however, their young and the middle disc components have very short $h_{z,\odot} \sim 40 \text{ pc}$. This suggests that the youngest disc in the Milky Way is confined to a very thin sheet like distribution. Therefore, that the younger part of our RC sample, though not as young as the young counterpart of BV24, has a short scale-height is perhaps not too surprising. The thicker component in our RC sample does have $h_{z,\odot} = 0.45$

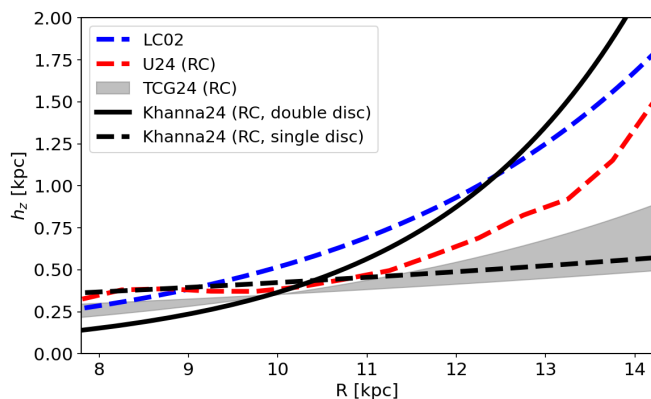


Fig. 29. Profile of scale-height as a function of R predicted from our best fit model (2 disc component) for *gdr3wise*[RC] as black solid curve, and for the 1 disc component as dotted black curve. The red and blue dotted curves show the profiles from two other studies of RC stars in literature, and in grey we show the profiles from TCG24 spanning from $[\text{Fe}/\text{H}] = -0.3$ (lower bound) to $[\text{Fe}/\text{H}] = 0.3$ (upper bound).

kpc, and this could be due some overlap with the high- α component of BV24. Using extremely precise stellar parameters from *Gaia* DR3 (*GSP-Spec*), Recio-Blanco et al. (2024) showed the presence of a bimodality in the RC on the *Kiel* diagram, that is suggested to map to the typical bimodality seen in $[\alpha/\text{Fe}]$ - $[\text{Fe}/\text{H}]$ separating the traditional thin and thick disc. Our Model 1 in Table 4 for just a single disc component predicts $h_{z,\odot} = 0.40$ kpc and $\log_{10} R_{\text{fl}} = 1.15$, and we have overplotted this in Figure 29 as a dashed black curve. It is interesting to note that between $8 < R < 11$ kpc, the profile is almost exactly identical to that found by U24, and also quite similar to the single exponential discs of TCG24. However, as noted earlier, this single disc model is unable to account for the stellar counts in the outer disc.

Aside from the flare, we also see a clear signature of the warp in the outer disc residuals (Figure 24), which we attempted to add to our model. While the resulting warp amplitude suggests that it may differ between young and old populations (Figure 28), we should bear in mind that, in this study at least, we are able to explore the warp only over a limited portion of the Galactic disc. However, the warp is a large-scale feature, and we therefore should avoid over-interpreting the warp amplitude obtained here. In any case, Figure 28 shows that our knowledge of the warp amplitude is quite uncertain, especially for the old populations. Moreover, we note that while the residuals in the outer disc (shown in Figure 27) are lower than those in the non-warped case, they do not disappear completely. This may be due in part to assuming an over-simplified warp geometry with a straight line of nodes. Nevertheless, our tests represent a first step in the right direction, confirming the warp signature in our RC sample, but there is still need for further exploration in future work.

In the previous section we also discussed the residuals between the two-disc model and the data projected on the Galactic plane (Figure 25), noting that they seem to show evidence of a two-arm spiral pattern with geometry similar to that inferred from NIR data (D00). In Figure 30 we show the residuals for $|Z_{\text{GC}}| < 1$ kpc also with the geometry of spiral arm models based on masers (Reid et al. 2019, hereafter R19) and the Cepheids (Drimmel et al. 2024). We find that the location of the outer residuals also roughly coincides with the location of the Outer Arm proposed by R19. The Perseus arm as mapped by the Cepheids and the HI (Levine et al. 2006) also cross this region,

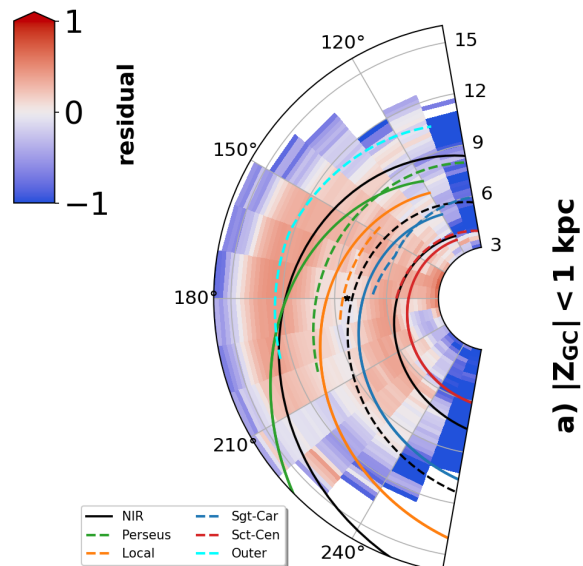


Fig. 30. Same as Figure 25 but for the $|Z_{\text{GC}}| < 1$ kpc slice. Various spiral arm models are overplotted: Coloured dashed lines show model based on masers from Reid et al. (2019), coloured solid lines show model based on Cepheids from Drimmel et al. (2024), and in black is the 2-arm NIR model from D00.

though with an apparently higher pitch angle. Recently Uppal et al. (2023) also claim to have detected the Outer Arm in a sample of RC stars selected using *Gaia* and 2MASS photometry using the overdensity mapping technique of Poggio et al. (2021). However, we note that the arm detected here in the RC residuals is much broader than the one they report. This is likely due to their choice of bandwidths for calculating the overdensity, restricting their sensitivity to features with scale lengths between 0.3 and 2 kpc. In addition, the overdensity mapping approach may be highlighting a small fraction of young stars transiting in their selected RC region of the colour-magnitude diagram as they evolve from the main sequence to the giant branch. Finally, though we note generally higher residuals in the first quadrant between $6 < R < 8$ kpc from $130^\circ < \phi < 160^\circ$, we do not detect a feature in the residuals that might correspond to the Local arm, especially near the disk midplane ($|Z_{\text{GC}}| < 0.25$ kpc, see middle panel of Figure 25), where the Local arm instead falls in an under-dense portion of the disc that lies along the expected inter-arm region of the NIR arms. This is in contrast with Lin et al. (2022), who also use the overdensity mapping approach for a selection of RC stars, and may suffer the same issues mentioned above.

In summary, if our residuals are mapping a spiral perturbation in the old stellar population, the geometry and profile of this perturbation is more consistent with a broad two-armed spiral than the multiple arms traced by young populations and star formation products (R19; Zari et al. 2021; Poggio et al. 2021, ,Gaia23). However, we should bear in mind that the residuals shown in Figure 25 might also be influenced by additional effects. For instance, any deviation of our best-fit parametrization (especially in the case of two or more disc-like components) with respect to the unknown true underlying density distribution might result in radial over/under-densities, which might interfere with interpreting any possible spiral arm signature. In addition,

an unaccounted for asymmetric warp may introduce additional residuals in the outer disc.

Nevertheless, that the geometry and width of the spirals as traced by the RC stars might not be the same as that seen in the young populations should not be a surprise. Presumably the RC population is tracing the old, kinematically relaxed stellar population that dominates the underlying mass distribution of the stellar disk, while young stars are a product of the response of the gas to a disc with multiple pattern speeds and, possibly, external perturbations (Purcell et al. 2011; Pettitt et al. 2016). If the residuals from our axisymmetric disc model are tracing a spiral perturbation in the old stellar disc of the Milky Way, their magnitude suggests that this perturbation is at the level of 10 to 20%. These residuals in the outer disc extend to a Galactocentric radius of at least 14-15 kpc, well beyond the outer Lindblad radius of the bar which is at a radius of 10-12 kpc based on recent estimates of the bar's pattern speed (Binney 2020; Chiba & Schönrich 2021; Dillamore et al. 2024; Lucchini et al. 2024, Gaia23), so that any spiral perturbation responsible for these residuals must have a lower pattern speed than the bar, as a spiral arm perturbation is expected to be located between its own inner and outer Lindblad resonances.

6. Summary

In this paper, we constructed an all-sky catalogue of RC candidates, for which we could derive reliable distances using MIR photometry from *AllWISE*. This sample of nearly 10 million stars allowed us to map the stellar number density for galactocentric radii between $3 < R \text{ [kpc]} < 14$ and at a distance from the Galactic midplane of $|Z_{GC}| < 2$ kpc. Taking advantage of the near Gaussian luminosity function of the RC and 3D extinction maps, we built a selection function tailored to our sample, i.e. the probability of observing an RC star at a given location on sky at a given magnitude. The selection function then allowed us to build a three dimensional completeness map of our sample and to fit a range of models to the observed stellar density. It is only by taking into account the selection function that we can use the RC sample to trace a large fraction of the Galactic disc. Indeed, limiting ourselves to a sample with 90% completeness would limit our volume to within only 2 to 4 kpc of the Sun (see Figure 20). Our best model consists of two discs, where each is exponential both radially and vertically. Specifically, the RC population of the Galaxy seems to be well described by a long and thin disc component that makes up about 36% of the stellar mass. It has a scale-length $R_d = 3.56$ kpc and scale-height at the Sun of $h_{z,\odot} = 0.17$ kpc, flaring to 2 kpc at $R = 14$ kpc. The remaining 64% of the mass is in a disc with a scale length of $R_d = 2.59$ kpc and a scale-height of $h_{z,\odot} = 0.45$ kpc without a flare. Beyond $R > 10$ kpc we find a clear signature of the Galactic warp. We show that for our dataset, the onset of the warp is around $R = 9$ kpc.

Subtracting the best-fit model from the data we find residuals in both the inner and the outer disc. These residuals seem to coincide with the expected location of the spiral arms inferred from the NIR (D00; Drimmel & Spergel 2001; Benjamin et al. 2005; Hou & Han 2015), corroborating the two-armed geometry implied by the observed spiral arm tangents at these wavelengths, and implying a perturbation in the mass surface density of 10 to 20%. To confirm these results will require a better modelling of the outer disk to fully take into account the warp, and/or a deeper catalogue toward the inner Galaxy where extinction still limits the volume we are able to sample.

We have here modelled the density of the RC stars with a purely geometrical model, which requires sufficient knowledge of the extinction in three dimensions as well as the combined selection function of the photometric surveys used. Because of these stringent conditions for mapping the three dimensional density in the Galactic plane, earlier attempts to verify the existence of a spiral perturbation in the mass density of the stellar disk have relied on the measured velocities of tracers (Grosbøl & Carraro 2018; Eilers et al. 2020). Recently, Palicio et al. (2023) detected spiral-like features in the radial action J_R of disc stars. However, since *Gaia* DR3 it has become clear that the bar of the Milky Way dominates the velocity field of the disc well beyond corotation (Gaia23), thus complicating any possible interpretation of the disc's velocity field. Nevertheless, we intend to study the velocities of the RC sample in the future. Indeed, including this additional information may allow us to better constrain the warp in this old stellar population.

Acknowledgements. SK & RD acknowledge support from the European Union's Horizon 2020 research and innovation program under the GaiaUnlimited project (grant agreement No 101004110). SK acknowledges use of the INAF PLEIADI@IRA computing resources (<http://www.pleiadi.inaf.it>), and Hai-Feng Wang for useful suggestions. RD is supported in part by the Italian Space Agency (ASI) through contract 2018-24-HH.0 and its addendum 2018-24-HH.1-2022 to the National Institute for Astrophysics (INAF). This work presents results from the European Space Agency (ESA) space mission Gaia. Gaia data are being processed by the Gaia Data Processing and Analysis Consortium (DPAC). Funding for the DPAC is provided by national institutions, in particular the institutions participating in the Gaia MultiLateral Agreement (MLA). The Gaia mission website is <https://www.cosmos.esa.int/gaia>. The Gaia archive website is <https://archives.esac.esa.int/gaia>. This work has used the following additional software products: TOPCAT, STIL, and STILTS (Taylor 2005); Matplotlib (Hunter 2007); IPython (Pérez & Granger 2007); Pandas (pandas development team 2020); Astropy, a community-developed core Python package for Astronomy (Astropy Collaboration et al. 2018); NumPy (Harris et al. 2020); and Vaex (Breddels & Veljanoski 2018).

References

- Abdurro'uf, Accetta, K., Aerts, C., et al. 2022, *ApJS*, 259, 35
- Andrae, R., Rix, H.-W., & Chandra, V. 2023, *ApJS*, 267, 8
- Astropy Collaboration, Price-Whelan, A. M., Sipőcz, B. M., et al. 2018, *AJ*, 156, 123
- Aumer, M. & Binney, J. 2017, *MNRAS*, 470, 2113
- Bailer-Jones, C. A. L. 2015, *PASP*, 127, 994
- Bailer-Jones, C. A. L., Rybizki, J., Fousneau, M., Demleitner, M., & Andrae, R. 2021, *AJ*, 161, 147
- Bedding, T. R., Mosser, B., Huber, D., et al. 2011, *Nature*, 471, 608
- Benjamin, R. A., Churchwell, E., Babler, B. L., et al. 2005, *ApJ*, 630, L149
- Bennett, M. & Bovy, J. 2019, *MNRAS*, 482, 1417
- Binney, J. 2020, *Monthly Notices of the Royal Astronomical Society*, 495, 895
- Binney, J. & Vasiliev, E. 2023, *MNRAS*, 520, 1832
- Binney, J. & Vasiliev, E. 2024, *MNRAS*, 527, 1915
- Bland-Hawthorn, J. & Gerhard, O. 2016, *ARA&A*, 54, 529
- Borucki, W. J., Koch, D., Basri, G., et al. 2010, *Science*, 327, 977
- Bovy, J., Bird, J. C., García Pérez, A. E., et al. 2015, *ApJ*, 800, 83
- Bovy, J., Rix, H.-W., Schlafly, E. F., et al. 2016, *ApJ*, 823, 30
- Breddels, M. A. & Veljanoski, J. 2018, *A&A*, 618, A13
- Buder, S., Sharma, S., Kos, J., et al. 2021, *MNRAS*, 506, 150
- Cabrera-Gadea, M., Mateu, C., Ramos, P., et al. 2024, *MNRAS*, 528, 4409
- Cannon, R. D. 1970, *MNRAS*, 150, 111
- Cantat-Gaudin, T., Fousneau, M., Rix, H.-W., et al. 2023a, *A&A*, 669, A55
- Cantat-Gaudin, T., Fousneau, M., Rix, H.-W., et al. 2023b, *A&A*, 669, A55
- Cantat-Gaudin, T., Fousneau, M., Rix, H.-W., et al. 2024, *A&A*, 683, A128
- Castro-Ginard, A., Brown, A. G. A., Kostrzewa-Rutkowska, Z., et al. 2023, *A&A*, 677, A37
- Chen, X., Wang, S., Deng, L., et al. 2019, *Nature Astronomy*, 3, 320
- Cheng, X., Anguiano, B., Majewski, S. R., et al. 2020, *ApJ*, 905, 49
- Chiba, R. & Schönrich, R. 2021, *MNRAS*, 505, 2412
- De Silva, G. M., Freeman, K. C., Bland-Hawthorn, J., et al. 2015, *MNRAS*, 449, 2604
- Dehnen, W., Semiczuk, M., & Schönrich, R. 2023, *MNRAS*, 523, 1556
- Deng, L.-C., Newberg, H. J., Liu, C., et al. 2012, *Research in Astronomy and Astrophysics*, 12, 735

- Dillamore, A. M., Belokurov, V., & Evans, N. W. 2024, *MNRAS*, 532, 4389
- Drimmel, R. 2000, *A&A*, 358, L13
- Drimmel, R., Khanna, S., Poggio, E., & Skowron, D. M. 2024, arXiv e-prints, arXiv:2406.09127
- Drimmel, R. & Spergel, D. N. 2001, *ApJ*, 556, 181
- Eilers, A.-C., Hogg, D. W., Rix, H.-W., et al. 2020, *ApJ*, 900, 186
- Elsworth, Y., Hekker, S., Johnson, J. A., et al. 2019, *MNRAS*, 489, 4641
- Foreman-Mackey, D., Hogg, D. W., Lang, D., & Goodman, J. 2013, *PASP*, 125, 306
- Frankel, N., Sanders, J., Ting, Y.-S., & Rix, H.-W. 2020, *ApJ*, 896, 15
- Gaia Collaboration, Antoja, T., McMillan, P. J., et al. 2021, *A&A*, 649, A8
- Gaia Collaboration, Brown, A. G. A., Vallenari, A., et al. 2016, *A&A*, 595, A2
- Gaia Collaboration, Drimmel, R., Romero-Gómez, M., et al. 2023, *A&A*, 674, A37
- Gilmore, G. & Reid, N. 1983, *MNRAS*, 202, 1025
- Girardi, L. 2016, *ARA&A*, 54, 95
- Gordon, K. D., Clayton, G. C., Decleir, M., et al. 2023, *ApJ*, 950, 86
- Gravity Collaboration, Abuter, R., Amorim, A., et al. 2021, *A&A*, 647, A59
- Green, G. M., Schlafly, E., Zucker, C., Speagle, J. S., & Finkbeiner, D. 2019, *ApJ*, 887, 93
- Grisoni, V., Chiappini, C., Miglio, A., et al. 2024, *A&A*, 683, A111
- Grosbøl, P. & Carraro, G. 2018, *A&A*, 619, A50
- Harris, C. R., Millman, K. J., van der Walt, S. J., et al. 2020, *Nature*, 585, 357
- Hawkins, K., Leistedt, B., Bovy, J., & Hogg, D. W. 2017, *MNRAS*, 471, 722
- Hayden, M. R., Bovy, J., Holtzman, J. A., et al. 2015, *ApJ*, 808, 132
- Hekker, S. & Christensen-Dalsgaard, J. 2017, *A&A Rev.*, 25, 1
- Hou, L. G. & Han, J. L. 2015, *MNRAS*, 454, 626
- Hunter, J. D. 2007, *Computing in Science & Engineering*, 9, 90
- Jónsson, V. H. & McMillan, P. J. 2024, *A&A*, 688, A38
- Jurić, M., Ivezić, Ž., Brooks, A., et al. 2008, *ApJ*, 673, 864
- Khanna, S., Sharma, S., Bland-Hawthorn, J., et al. 2019a, *Monthly Notices of the Royal Astronomical Society*, 482, 4215
- Koch, D. G., Borucki, W. J., Basri, G., et al. 2010, *ApJ*, 713, L79
- Koppelman, H. H. & Helmi, A. 2021, *A&A*, 645, A69
- Lallement, R., Babusiaux, C., Vergely, J. L., et al. 2019, *A&A*, 625, A135
- Levine, E. S., Blitz, L., & Heiles, C. 2006, *Science*, 312, 1773
- Li, C. & Binney, J. 2022, *MNRAS*, 516, 3454
- Lian, J., Zasowski, G., Chen, B., et al. 2024, arXiv e-prints, arXiv:2406.05604
- Lin, Z., Xu, Y., Hou, L., et al. 2022, *The Astrophysical Journal*, 931, 72
- Lindgren, L., Bastian, U., Biermann, M., et al. 2021, *A&A*, 649, A4
- López-Corredoira, M., Cabrera-Lavers, A., Garzón, F., & Hammersley, P. L. 2002, *A&A*, 394, 883
- Lucchini, S., D’Onghia, E., & Aguerri, J. A. L. 2024, *MNRAS*, 531, L14
- Lucey, M., Ting, Y.-S., Ramachandra, N. S., & Hawkins, K. 2020, *MNRAS*, 495, 3087
- Luri, X., Brown, A. G. A., Sarro, L. M., et al. 2018, *A&A*, 616, A9
- Majewski, S. R., Schiavon, R. P., Frinchaboy, P. M., et al. 2017, *AJ*, 154, 94
- Marrese, P. M., Marinoni, S., Fabrizio, M., & Altavilla, G. 2019, *A&A*, 621, A144
- Ness, M., Freeman, K., Athanassoula, E., et al. 2012, *ApJ*, 756, 22
- Palicio, P. A., Recio-Blanco, A., Poggio, E., et al. 2023, *A&A*, 670, L7
- pandas development team, T. 2020, *pandas-dev/pandas: Pandas*
- Pérez, F. & Granger, B. E. 2007, *Computing in Science and Engineering*, 9, 21
- Pettitt, A. R., Tasker, E. J., & Wadsley, J. W. 2016, *MNRAS*, 458, 3990
- Pietrzyński, G., Graczyk, D., Gallenne, A., et al. 2019, *Nature*, 567, 200
- Poggio, E., Drimmel, R., Cantat-Gaudin, T., et al. 2021, *A&A*, 651, A104
- Poggio, E., Khanna, S., Drimmel, R., et al. 2024, arXiv e-prints, arXiv:2407.18659
- Purcell, C. W., Bullock, J. S., Tollerud, E. J., Rocha, M., & Chakrabarti, S. 2011, *Nature*, 477, 301
- Queiroz, A. B. A., Anders, F., Chiappini, C., et al. 2023, *A&A*, 673, A155
- Randich, S., Gilmore, G., & Gaia-ESO Consortium. 2013, *The Messenger*, 154, 47
- Recio-Blanco, A., de Laverny, P., Palicio, P. A., et al. 2024, arXiv e-prints, arXiv:2402.01522
- Reid, M. J., Menten, K. M., Brunthaler, A., et al. 2019, *ApJ*, 885, 131
- Rix, H.-W. & Bovy, J. 2013, *A&A Rev.*, 21, 61
- Rix, H.-W., Hogg, D. W., Boubert, D., et al. 2021, *AJ*, 162, 142
- Robin, A. C., Reylé, C., Derrière, S., & Picaud, S. 2003a, *A&A*, 409, 523
- Robin, A. C., Reylé, C., Derrière, S., & Picaud, S. 2003b, *A&A*, 409, 523
- Ruiz-Dern, L., Babusiaux, C., Arenou, F., Turon, C., & Lallement, R. 2018, *A&A*, 609, A116
- Rybizki, J., Demleitner, M., Bailer-Jones, C., et al. 2020, *PASP*, 132, 074501
- Schlafly, E. F., Green, G. M., Lang, D., et al. 2018, *ApJS*, 234, 39
- Schlafly, E. F., Meisner, A. M., & Green, G. M. 2019, *ApJS*, 240, 30
- Schlegel, D. J., Finkbeiner, D. P., & Davis, M. 1998, *ApJ*, 500, 525
- Sharma, S., Bland-Hawthorn, J., Johnston, K. V., & Binney, J. 2011, *ApJ*, 730, 3
- Skowron, D. M., Skowron, J., Mróz, P., et al. 2019, *Acta Astron.*, 69, 305
- Skrutskie, M. F., Cutri, R. M., Stiening, R., et al. 2006, *AJ*, 131, 1163
- Steinmetz, M., Matijević, G., Enke, H., et al. 2020, *AJ*, 160, 82
- Taylor, M. B. 2005, in *Astronomical Society of the Pacific Conference Series*, Vol. 347, *Astronomical Data Analysis Software and Systems XIV*, ed. P. Shopbell, M. Britton, & R. Ebert, 29
- Ting, Y.-S., Hawkins, K., & Rix, H.-W. 2018, *ApJ*, 858, L7
- Uppal, N., Ganesh, S., & Schultheis, M. 2023, *A&A*, 673, A99
- Uppal, N., Ganesh, S., & Schultheis, M. 2024, *MNRAS*, 527, 4863
- Vasiliev, E. 2018, arXiv e-prints, arXiv:1802.08255
- Vasiliev, E. 2019, *MNRAS*, 482, 1525
- Vislosky, E., Minchev, I., Khoperskov, S., et al. 2024, *MNRAS*, 528, 3576
- Wang, H. F., López-Corredoira, M., Huang, Y., et al. 2020, *ApJ*, 897, 119
- Warfield, J. T., Zinn, J. C., Schonhut-Stasik, J., et al. 2024, arXiv e-prints, arXiv:2403.16250
- Wegg, C. & Gerhard, O. 2013, *MNRAS*, 435, 1874
- Wright, E. L., Eisenhardt, P. R. M., Mainzer, A. K., et al. 2010, *AJ*, 140, 1868
- Yoshii, Y. 1982, *PASJ*, 34, 365
- Yu, J., Casagrande, L., Ciucă, I., et al. 2024, *MNRAS*, 530, 2953
- Yu, J., Huber, D., Bedding, T. R., et al. 2018, *ApJS*, 236, 42
- Zari, E., Rix, H. W., Frankel, N., et al. 2021, *A&A*, 650, A112

Table B.1. Best-fit coefficients for equation B.6 used to derive $(J - K)_0$ for Giants and the Red Clump in K19. The fitting was carried out over the temperature range $4200 < T_{\text{eff}} < 8000$.

| Population | a_0 | a_1 | a_2 | a_3 | a_4 | a_5 |
|------------|--------|-------|--------|--------|-------|-------|
| Giants | -0.957 | 0.000 | -0.006 | -0.020 | 1.489 | 0.002 |
| Red Clump | -0.800 | 0.046 | 0.008 | -0.060 | 1.199 | 0.132 |

Appendix A: Distance Posterior Probability distribution (PDF) from *CBJ21*

For clarity, we reproduce here the relations to obtain the posterior PDF from *CBJ21*. The geometric distance prior is written in the form of a Generalized Gamma distribution (GGD),

$$P(r|hpix) = \frac{1}{\Gamma(\frac{\beta+1}{\alpha})} \frac{\alpha}{L^{\beta+1}} r^{\beta} e^{-(r/L)\alpha}, \quad (\text{A.1})$$

valid for distance, $r \geq 0$. Given a HEALpixel (level 5), $hpix$, one can obtain the parameters α, β , and L from the auxiliary file provided by *CBJ21*. Then, using the likelihood function,

$$P(\varpi'|r, \sigma_{\varpi}) = \mathcal{N}(\varpi' - \frac{1}{r}, \sigma_{\varpi}), \quad (\text{A.2})$$

where $\varpi' = \varpi + 0.017$, we can write the posterior PDF, as a product of the likelihood and the prior, as

$$P_g(r|\varpi', \sigma_{\varpi}, hpix) = P(\varpi'|r, \sigma_{\varpi})P(r|hpix) \quad (\text{A.3})$$

Appendix B: RC Validation

Appendix B.1: Selecting Red clump from Stellar Parameters

In this paper, our *gdr3wise*[RC] sample is selected by combining *Gaia* astrometry & photometry with *AllWISE* photometry. Ultimately however, a purer sample of RC stars can be selected using spectroscopic stellar parameters ($\log g$, $[\text{Fe}/\text{H}]$, T_{eff}). In K19, we had developed such a scheme to select high fidelity RC stars, and we provide a short summary of this below:

$$1.8 \leq \log g \leq 0.0018 \text{ dex K}^{-1} (T_{\text{eff}} - T_{\text{eff}}^{\text{ref}}([\text{Fe}/\text{H}])) + 2.5, \quad (\text{B.1})$$

$$Z > 1.21[(J - K)_0 - 0.05]^9 + 0.0011, \quad (\text{B.2})$$

$$Z < \text{Min}(2.58[(J - K)_0 - 0.40]^3 + 0.0034, 0.06), \quad (\text{B.3})$$

$$0.5 < (J - K)_0 < 0.8, \quad (\text{B.4})$$

where,

$$T_{\text{eff}}^{\text{ref}}([\text{Fe}/\text{H}]) = -382.5 \text{ K dex}^{-1} [\text{Fe}/\text{H}] + 4607 \text{ K}. \quad (\text{B.5})$$

and $Z = Z_{\odot} 10^{[\text{Fe}/\text{H}]}$, with $Z_{\odot} = 0.019$. Here, $(J - K)_0$ is the intrinsic colour in 2MASS passbands for RC stars. One can derive the intrinsic colour solely from stellar parameters as,

$$(J - K)_0 = a_0 + a_1 X + a_2 X^2 + a_3 XY + a_4 Y + a_5 Y^2, \quad (\text{B.6})$$

where $X = [\text{Fe}/\text{H}]$ and $Y = 5040 \text{ K}/T_{\text{eff}}$, and the coefficients as listed in Table B.1.

A23: In this paper, we only use the relations above for validation. In particular, we select RC candidates from the recently published stellar parameter catalogue of Andrae et al. (2023)(A23) who derived these for *Gaia* stars with XP spectra and CatWISE photometry (about 175 million in all). We are able to select 6,840,662 RC like stars from their catalogue, and find that 62% of these are present in *gdr3wise*[RC]. Figure B.1 shows

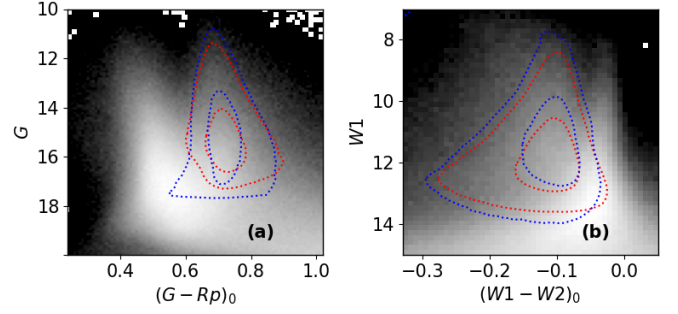


Fig. B.1. colour Magnitude diagram for the *gdr3wise* parent catalogue shown for *Gaia* and *AllWISE* colours. In each panel, we indicate the selected RC sample using the red contours ($1\sigma, 2\sigma$). Also, shown in blue contours are the spectroscopically selected RC from A23.

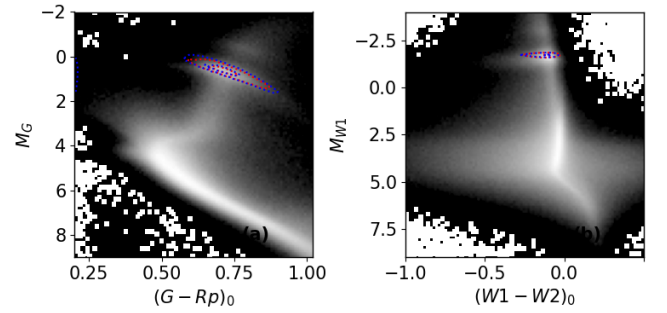


Fig. B.2. Colour-absolute magnitude diagram (CaMD) for the *gdr3wise* dataset, with M_G vs. $(G - G_{\text{RP}})_0$ shown in panel (a), and M_{W1} vs. $(W1 - W2)_0$ shown in panel (b). The red contours in each panel represent the selected *gdr3wise*[RC] stars. Also, shown in blue contours are the spectroscopically selected RC from A23.

the CMD in both *Gaia* and *AllWISE* colours for the *gdr3wise* parent sample in grey, with the *gdr3wise*[RC] shown as red contours and the sample selected from A23 in blue contours. In Figure B.2 we use the distance priors from *CBJ21* to show the CaMD for these in both *Gaia* and *AllWISE* colours, with the two RC samples once again indicated by red and blue contours. Our photo-astrometrically selected RC and that spectroscopically selected from A23 trace very similar distributions in these figures, though our selection is a bit more conservative, covering a smaller area in $(\log g, T_{\text{eff}})$ space.

APOGEE & GALAH: Next we consider the two main contemporary high resolution spectroscopic surveys *APOGEE* (Abdurro'uf et al. 2022, DR17) and *GALAH* (Buder et al. 2021, DR3). For each, we use their internal crossmatches to *Gaia* EDR3 source_id. We find about 150,000 of our RC sources in common with the two surveys combined. The *Kiel* diagram for *APOGEE* & *GALAH* surveys is shown in Figure B.3, with our RC selection overlaid as contours at $(1, 2)\sigma$, which lie within $1.8 < \log g < 3.0$. Interestingly, in both comparisons, we also note the presence of an overdensity around $(T_{\text{eff}}, \log g) = (5100 \text{ K}, 2.9)$. This would be the secondary Red Clump population, which are more massive and younger counterparts to the typical RC, burning helium in their cores after leaving the RGB without having experienced a helium flash (Girardi 2016).

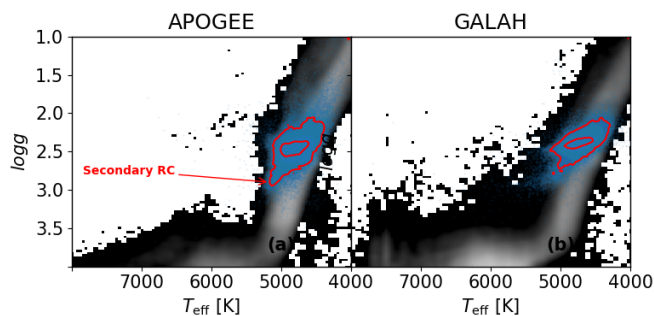


Fig. B.3. External validation of *gdr3wise*[RC] against the spectroscopic catalogues, *APOGEE* (panel a) and *GALAH* (panel b). For each survey we show the overall *Kiel* diagram, with the common sources in our catalogue overplotted (blue points). Also, shown is the $(1,2)\sigma$ density contours for the common sources. Note: the presence of an overdensity around $(T_{\text{eff}}, \log g) = (5100 \text{ K}, 2.9)$, which is likely the secondary Red Clump population.

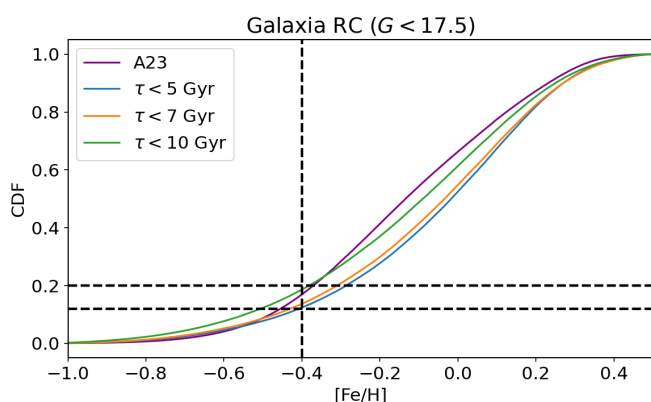


Fig. B.4. Cumulative distribution function (CDF) of the metallicity of RC population selected from *Galaxia* for a magnitude limited survey at $G < 17.5$. Three CDF curves are shown, each for a cut in maximum stellar age at $\tau = (5, 7, 10)$ Gyr. The horizontal black lines indicate $\text{CDF} = (0.12, 0.2)$, while the vertical black line indicates $[\text{Fe}/\text{H}] = -0.4$. Also shown is the CDF for the spectroscopically selected RC from A23.

Appendix B.2: Selecting RC in Galaxia & Metallicity CDF

In order to look at properties of RC stars, we generated an all-sky mock catalogue with magnitude limit of $G < 17.5$, using the *Galaxia* population synthesis code (Sharma et al. 2011), which implements the *Besancon* Galaxy model (Robin et al. 2003b). The *warpflare* option was set to 1. *Galaxia* allows sampling of stars in a continuous fashion across the sky, and also provides photometry, in most of the commonly used bands. From the mock, we selected RC stars using the scheme laid out in subsection B.1. Additionally, we select only those stars that have an initial stellar mass greater than their RGB tipping mass, and that are present in the Galactic disc. The *CaMD* in both *Gaia* and *AllWISE* colours is shown in Figure 2, with the RC population indicated as black contours. For this sample, the Cumulative Distribution Function (CDF) of their metallicity in Figure B.4 for three cuts in stellar age at $\tau = (5, 7, 10)$ Gyr is shown in Figure B.4, where we see that in general the fraction of stars with $[\text{Fe}/\text{H}] < -0.4$ ranges around 15-20% for the typical ages of RC stars ($\tau < 5$ Gyr). For completion, Figure B.4 also shows the metallicity CDF of RC that we select from A23 (purple curve), and this is consistent with that seen in *Galaxia*.

Appendix B.3: Comparison with Asteroseismology

In general the selection scheme laid out in subsection B.1 should be able to select high fidelity RC stars, however given the close overlap with the RGB and secondary RC populations in both photometric and spectroscopic spaces, it is easy to also select contaminants. The gold-standard for distinguishing between these phases of stars is asteroseismology - the study of stellar oscillations. This technique is sensitive to the internal structure of stars, and thus allows one to select pure RC stars. In red giant stars, these oscillations are excited by near-surface convection, and are broadly characterised as two dominant modes: a) acoustic (p -mode): the propagation zone of such modes is the outer envelope of the star, with pressure acting as the restoring force. Observationally, these modes are approximately equally spaced in oscillation frequency; b) gravity (g -mode): such modes propagate in the interior of the core, and buoyancy acts as the restoring force here. Pure g -modes are approximately equally spaced in their period. In evolved stars, coupling between the p and g modes results in the so called mixed modes. In their seminal work, Bedding et al. (2011) showed that such mixed modes in red giant stars can help distinguish between the RGB and the RC phases.

This relies on their different distributions in the $\Delta\nu$ - ΔP plane. Here, $\Delta\nu$ is the frequency separation between adjacent p -modes with the same angular degree but at different radial order, while ΔP is the period spacing between adjacent mixed modes. Fundamentally, this is due to the differences in the structure of the cores of the two types. While, RGB have a radiative core, RC stars have a fully convective core. It turns out that mixed modes cannot stably propagate through convective cores, but can do so in the radiative regions above the core in RC stars. Since, the radiative region in RC stars is smaller compared to RGB stars, this has the consequence of larger PS , thus making it a key discriminant between the two stellar phases (Hekker & Christensen-Dalsgaard 2017). We now compare our sample to three independent publicly available catalogues that use asteroseismology to classify stellar phases. For each of the following, we provide the precision, recall and accuracy, as quality markers, defined as Precision = (True positive/Results), Recall = (True positive/ True positive + False Negative), and Accuracy = (True positive + True Negative) / (Total - Unclassified).

Yu et al. (2018, Yu18 hereafter) carried out an extensive asteroseismic analysis on a sample of 16,094 red giants with light curves from the *Kepler* Space Telescope (Borucki et al. 2010; Koch et al. 2010). In addition to global seismic parameters, their catalogue also provides a classification for the stellar phase, given as, [0: ‘unclassified’ (706), 1: RGB (7685), 2: RC (7703)], with the number of each quoted in bold. We make use of the 1 arcsec spatial crossmatch performed for *Kepler* stars with *Gaia* DR2, provided by *gaia-kepler.fun*⁷. Then, using the *gaiaedr3.dr2_neighbourhood* table, we download the *Gaia* EDR3 source identifier (ID) for the Yu18 sample. We find 7491 stars in common between our catalogue and Yu18, out of which 82% were classified as phase 2 by the latter. Taking into account the ‘impurity’ (RGB) in our sample, with respect to Yu18, our selection achieves an accuracy also of about 82%.

Elsworth et al. (2019, Els19 hereafter) : In the literature, one finds a diverse range of techniques employed in the classification of the stellar phase of oscillating giants, and the results are also varied. Els19 compiled a ‘consensus’ evolutionary state for 6000 red giant stars, from four different methods of analysing the frequency-power spectrum. This sample has

⁷ <https://gaia-kepler.fun/>

been observed by *Kepler*, and also by the *APOGEE* and/or *SDSS* surveys. In their catalogue, they assign the following primary classifications, 'RGB' (red giant branch), 'RC' (red clump), '2CL' (secondary red clump), 'AGB' (asymptotic giant branch), and, 'U' (unclassified). Additionally, some stars are assigned a combination of these classifications, i.e., '2CL/U', 'AGB/U', 'RC/2CL', 'RC/U', 'RGB/AGB', 'RGB/U'. We obtain the *Gaia* EDR3 source IDs for Els19, following the exact same crossmatching procedure as we did for Yu18. Next, we select three populations, namely, a) **RC**: where 'consensus'=='RC'|'RC/2CL'|'RC/U'|'2CL'|'2CL/U', b) **RGB**: where 'consensus'=='AGB/U'|'RGB'|'RGB/AGB'|'RGB/U'|'U', and, c) **Unclassified**: where consensus=='U'. We find 1376 stars in common with Els19, out of which, 74% are classified as RC by the latter. Taking into account the impurity (RGB), we still achieve an accuracy of about 71%, though we of course note the lower completeness compared to Yu18.

Lucey et al. (2020, L20 hereafter) L20 put out a photometric catalogue of 2.6 million RC candidates. Their method involves predicting asteroseismic parameters (PS , $\Delta\nu$) and stellar parameters ($\log g$, T_{eff}) from spectral energy distributions (SED), using a neural network trained on RC stars from Ting et al. (2018). They combined photometry from *Pan-STARRS*, *AllWISE*, *2MASS*, and *Gaia* DR2. In their catalogue, they provide two sets of RC samples: a) 'Tier 2': 2,210,769 candidates with a contamination rate of $\approx 33\%$, and b) 'Tier 1': A superior set of 405,231, with a lower contamination rate of $\approx 20\%$. For our comparison we restrict to their stricter 'Tier 1' sample. As before, we make use of the *gaiaedr3.dr2_neighbourhood* table to recover the corresponding *Gaia* EDR3 source IDs for all stars in the L20 catalogue. In Figure B.5, we illustrate the comparison between *gdr3wise*[RC] and L20 on the *Kiel* diagram, using stellar parameters from the latter. In Figure B.5(a) we show all the red clump candidates (Tier 1 and Tier 2), from L20, and the 1, 2, and 3 σ density contours are shown in black. Also, marked are typical crude boundaries, $1.8 < \log g < 3.0$, used to select RC, shown as a guide to the reader. We notice the presence of a skew in the density distribution, at lower $\log g$ values, beyond the lower end of this crude boundary. Next, in Figure B.5(b), we show the stars in common between L20 and *gdr3wise*[RC], where we note that the common selection lies well within the crude boundary, and in a tight locus in $\log g$. It is quite clear that our selection is a bit more conservative, and at the cost of accuracy, we miss out on possible contaminants in the L20 catalogue. Finally, in Figure B.5(c), we plot those stars which are classified as 'nan' in L20, but are present in our selection scheme. It is interesting to note that the stellar parameters for these from L20 are consistent with these being part of the red clump, although there are possible contaminants present, especially in the region with $\log g > 3$ and $T_{\text{eff}} > 5000$ K. Since our selection method relies on both updated astrometry and photometry from *Gaia* EDR3, as well as *AllWISE*, we are fairly confident that a large fraction of these are consistent with being members of the RC.

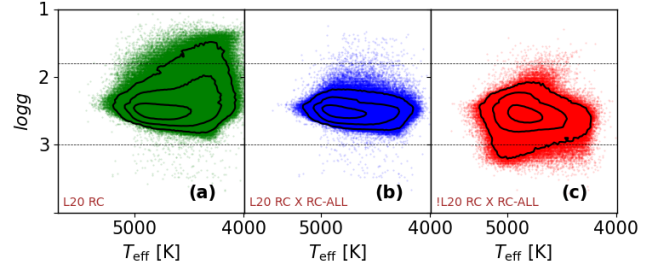


Fig. B.5. External validation of our catalogue (RC-ALL here) by cross-matching against the catalogue of L20, shown on the *Kiel* diagram using parameters from the latter. We also overplot density contours at $(1,2,3)\sigma$, shown in black. The typical crude boundary for RC stars, $1.8 < \log g < 3.0$ is indicated by black dotted lines. Panel (a) shows that the distribution of L20 falls mostly $(1,2)\sigma$ inside the crude boundaries, and is also broad in T_{eff} . Panel (b) shows the crossmatch between L20 and our sample. Nearly all of these overlapping sources lie between the crude boundary, and also display a tighter distribution in $\log g$. Panel (c), finally shows the stars that are present in L20, and are not classified as RC, but are present in our sample. Again, the stellar parameters from L20 for those that lie within the $(1,2)\sigma$ contour are consistent with expected boundaries, although there are possible contaminants around the region $\log g > 3$ and $T_{\text{eff}} > 5000$ K.

```

1 | SELECT healpix_, phot_g_mean_mag_, COUNT(*) AS n,
   | SUM(selection) AS k
2 | FROM (SELECT
   | to_integer(GAIA_HEALPIX_INDEX(5,source_id)) AS
   | healpix_, to_integer(floor((phot_g_mean_mag -
   | 3)/1.)) AS phot_g_mean_mag_,
3 | to_integer(IF_THEN_ELSE(wisenb.source_id
   | >0,1.0,0.0) ) AS selection
4 | FROM gaiadr3.gaia_source as gdr3
   | left outer join
5 | gaiadr3.allwise_best_neighbour as wisenb USING
   | (source_id)
6 | WHERE phot_g_mean_mag > 3 AND phot_g_mean_mag < 20
   | AND g_rp > -1 AND g_rp < 3.0 and parallax is
   | not null) AS subquery
7 | GROUP BY healpix_, phot_g_mean_mag_

```

In Figure C.1 we show the on sky projection of this sub-selection function for two magnitude bins, one at the bright end ($12 < G < 13$) where most of the sky has a high degree of completeness (though with noise due to small number statistics), and another at the faint end ($16 < G < 17$) where it is much less so. The reduced completeness near the Galactic plane and toward the inner Galaxy, as well as toward the Large and Small Magellanic Clouds, is mainly due to crowding and the low resolution of *AllWISE*.

Appendix C: Sub-selection function queries: Gaia X AllWISE

To build the sub-selection function layer of the selection function, we compute the ratio of sources that end up in the *gdr3wise* crossmatch vs. all sources in *Gaia*. We compute this ratio as a function of sky position (at *HEALPix* level 5), and G (1 magnitude wide bins). To this end, we ran the following query on the *Gaia* archive:

Appendix D: Corner Plots for Mock cases:

We show here the corner plots of the MCMC fit (1000 iterations) carried out on the two mock cases described in subsection 4.1. In case I we demonstrate the fit on an exponential disc with scale-height R_d , scale-length $h_{z,\odot}$, and a flare scale-length R_f (Figure D.1). In case II, we generate a mock galaxy identical to that in case I, except that it is also forced to be warped, and is described by four additional parameters (ϕ_w, R_w, h_{w0}, a_w) as shown in Figure D.2.

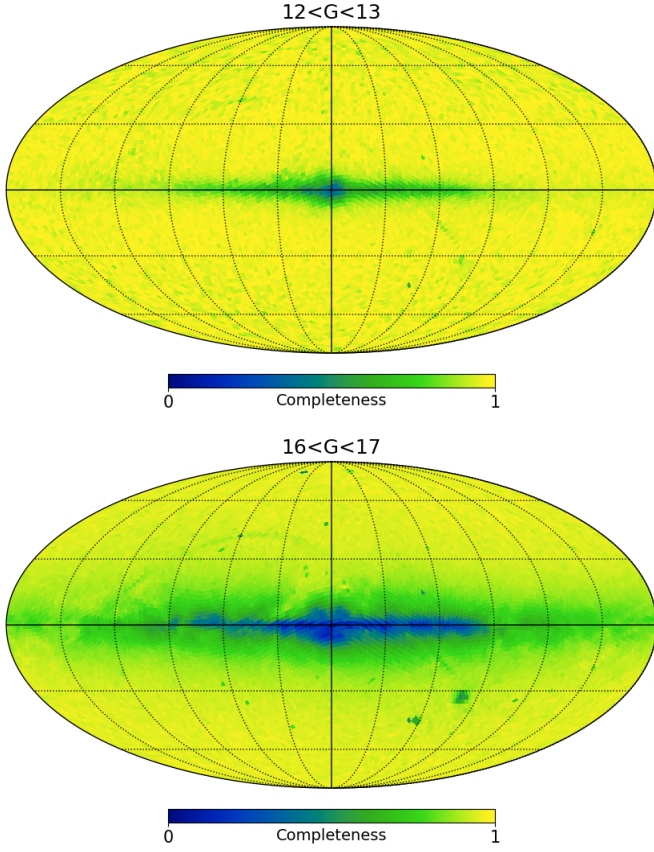


Fig. C.1. Completeness map for the sub-selection layer for *gdr3wise* dataset at *HEALPix* level 5, shown for a bright (top) and a faint magnitude bin (bottom).

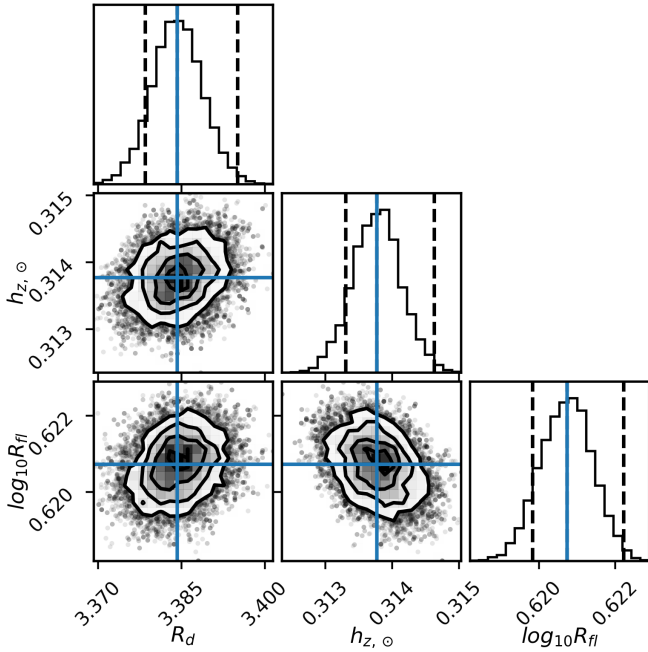


Fig. D.1. mock case I: Corner plots from the MCMC fitting for the three parameters describing mock case I, with the best fitting values indicated as vertical lines. The true values for this example are: $R_d = 3.3$ kpc, $h_{z,\odot} = 0.3$ kpc, $\log_{10} R_{fl} = 0.6$

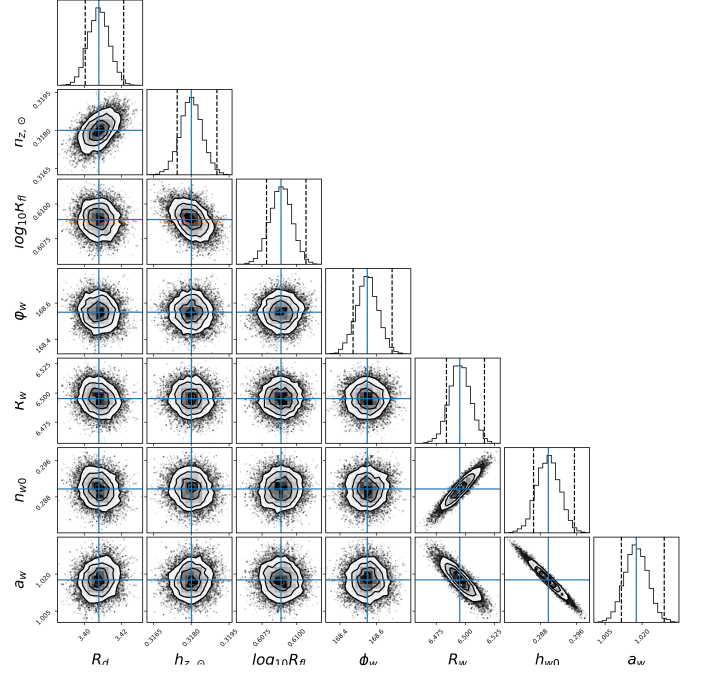


Fig. D.2. mock case II: Corner plots from the mcmc fitting for the three parameters describing mock case I, with the best fitting values indicated with blue lines. The true values in this example are: $R_d = 3.3$ kpc, $h_{z,\odot} = 0.3$ kpc, $\log_{10} R_{fl} = 0.6$, $\phi_w = 170^\circ$, $R_w = 6.5$ kpc, $a_w = 1.0$, $h_{w0} = 0.3$ kpc.

Appendix E: Corner plot: Single disc fit

Figure E.1 shows the corner plot for the fit to the *gdr3wise*[RC] dataset, for the case assuming only one disc component. Here we fit for the scale-length, scale-height and flare parameter only (see Model 1 in Table 4). The residuals for this fit are shown in Figure E.2 in ϕ - Z_{GC} projection for the inner ($3 < R < 10.5$ kpc) and the outer disc regions ($9.5 < R < 14.5$ kpc). Compared to the residuals for the double disc case shown in Figure 23, & Figure 24, this model does not fit the disc well across all R , and is especially problematic in the outer disc region.

Appendix F: Corner plot: Double disc fit

Figure F.1 shows the corner plot for fit to the *gdr3wise*[RC] dataset, assuming a double disc model. Here we fit for the scale-length, scale-height of two independent exponential discs, with one of these allowed to flare (see Model 2 in Table 4). We do not fit for the warp in this model.

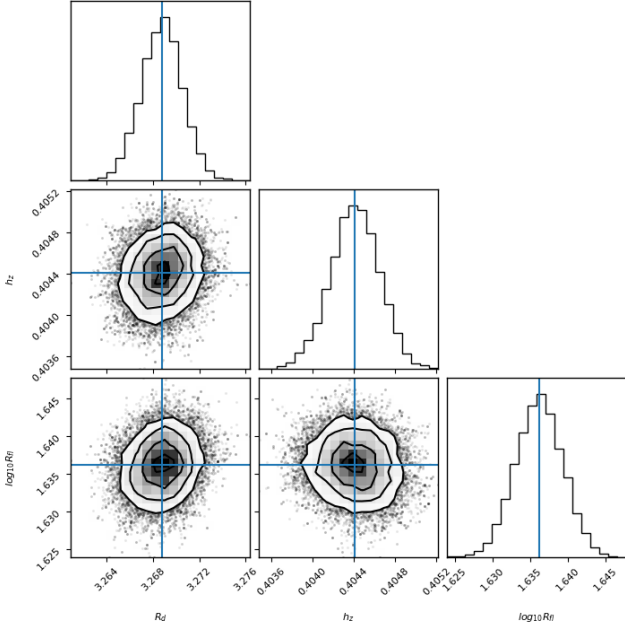


Fig. E.1. Posterior probability distributions for Model 1 (Table 4), applied to *gdr3wise*[RC]. This model allows for only one disc component.

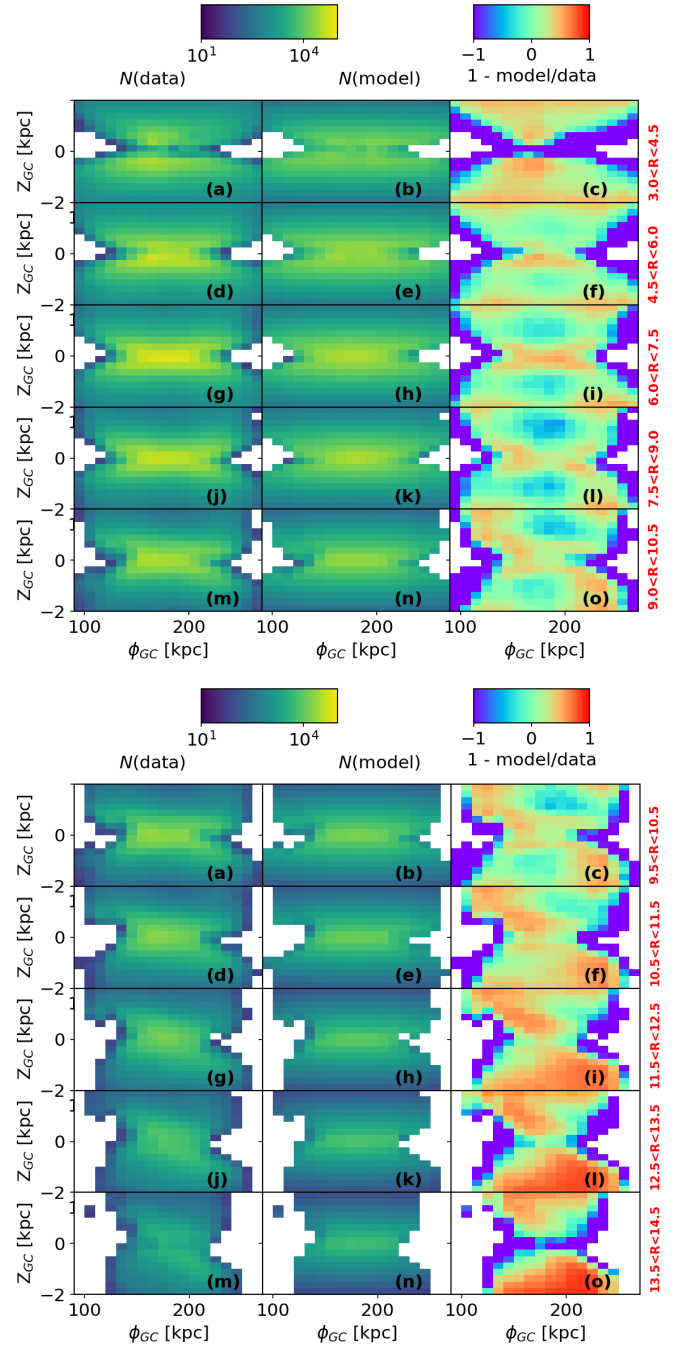


Fig. E.2. Residuals between the model and data in the ϕ, Z_{GC} projection, same as Figure 23 for the inner disc and Figure 24 for the outer disc, but for Model 1 i.e. that allows for only a single disc component (Table 4).

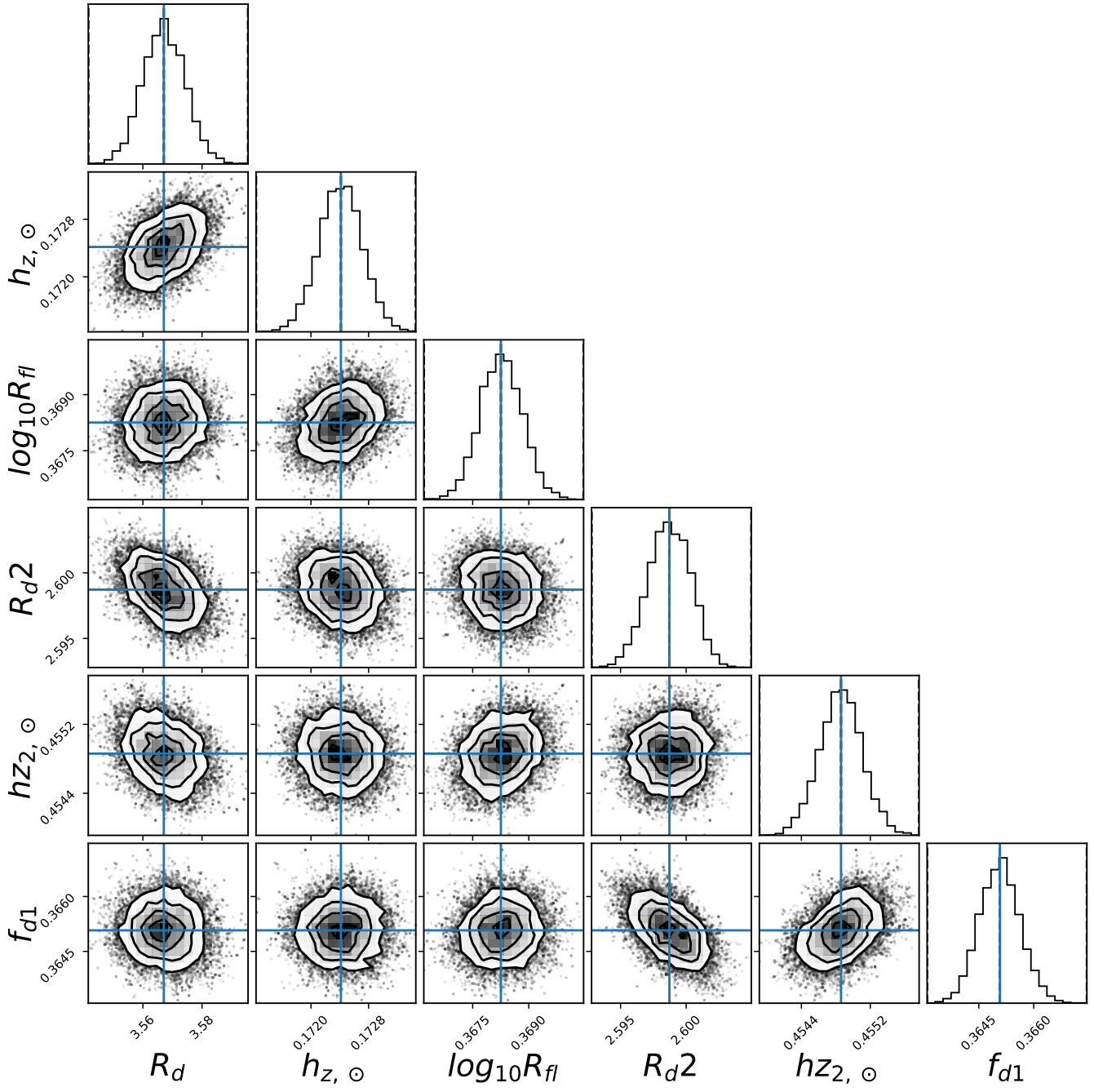


Fig. F.1. Posterior probability distributions for Model 2 (Table 4), applied to *gdr3wise*[RC]. This model allows for two discs.